UNIVERSIDADE FEDERAL DE SANTA CATARINA
PROGRAMA DE PÓS-GRADUAÇÃO EM CIÊNCIA E
ENGENHARIA DE MATERIAIS

Pietra Fagundes Araújo

INFLUENCE OF SINTERING CONDITIONS ON MICROSTRUCTURE AND PROPERTIES OF ALUMINA-FILLED BOROSILICATE GLASS

Florianópolis
2015

Pietra Fagundes Araújo

INFLUENCE OF SINTERING CONDITIONS ON MICROSTRUCTURE AND PROPERTIES OF ALUMINA-FILLED BOROSILICATE GLASS

Dissertação submetida ao Programa
de Pós-Graduação em Ciência e Engenharia
de Materiais para a obtenção
do Grau de Mestre em Ciência e Engenharia
de Materiais

Orientador: Dachamir Hotza
Coorientador: Daniel E. Garcia

Florianópolis
2015

Ficha de identificação da obra elaborada pelo autor,
através do Programa de Geração Automática da Biblioteca Universitária da UFSC.

Araújo, Pietra
INFLUENCE OF SINTERING CONDITIONS ON MICROSTRUCTURE AND PROPERTIES OF ALUMINA-FILLED BOROSILICATE GLASS / Pietra Araújo ; orientador, Dachamir Hotza ; coorientador, Daniel Garcia. - Florianópolis, SC, 2015.
134 p.

Dissertação (mestrado) - Universidade Federal de Santa Catarina, Centro Tecnológico. Programa de Pós-Graduação em Ciência e Engenharia de Materiais.

Inclui referências

1. Ciência e Engenharia de Materiais. 2. Ceramic-filled glass. 3. Borosilicate glass. 4. Sintering. 5. Fast firing. I. Hotza, Dachamir . II. Garcia, Daniel. III. Universidade Federal de Santa Catarina. Programa de Pós Graduação em Ciência e Engenharia de Materiais. IV. Título.

Pietra Fagundes Araújo

INFLUENCE OF SINTERING CONDITIONS ON MICROSTRUCTURE AND PROPERTIES OF ALUMINA-FILLED BOROSILICATE GLASS

Esta Tese foi julgada adequada para obtenção do Título de “Mestre em Ciência e Engenharia de Materiais”, e aprovada em sua forma final pelo Programa de Pós-Graduação em Ciência e Engenharia de Materiais da Universidade Federal de Santa Catarina.

Florianópolis, 28 de setembro de 2015

Prof. Dr. Antonio Pedro Novaes de Oliveira
Coordenador do Programa

Banca Examinadora:

Prof. Dr. Dachamir Hotza
Orientador
EQA/UFSC

Dr. Daniel E. Garcia
Coorientador

Prof. Dr. Márcio Fredel
EMC/UFSC

Dr. João Cardoso de Lima
FSC/UFSC

Dr. Hansu Birol
CSEM

Aos meus pais, Zaira e Lídio,
com muito orgulho.

AGRADECIMENTOS

Primeiramente agradeço a Deus que me deu forças para concluir esta dissertação.

A toda minha família, especialmente meus pais, Zaira e Lidio, meus irmãos Lucas e Monirée, e meu sobrinho Pietro, que me apoiaram ao longo destes dois anos, por me proporcionar, principalmente, apoio emocional.

Ao meu orientador Dachamir Hotza, por me dar a oportunidade de realizar este mestrado e por sua incrível dedicação para com todos.

Ao meu co-orientador e amigo Daniel E. Garcia por toda atenção, paciência e conhecimento transmitido. Por me ensinar a crescer profissionalmente, por todo apoio, confiança e esforço para o melhor desenvolvimento e concretização deste trabalho.

À minha querida amiga e IC Francesca Albino, por toda a dedicação e carinho.

Às minhas estagiárias, Mariana Souza, Livia Daros e Dandara Lodetti por toda a ajuda imprescindível.

Aos meus companheiros de trabalho e amigos Patrícia, Rafael, H. Tajiri, Mariana, Priscila, Useche, Daniel G., César, Marcelo, Joana, Sérgio, Tatiane, A. Cabral pessoas especiais que sempre estiveram por perto para tirar minhas dúvidas, ajudar e para descontrair.

Ao CERMAT, que se tornou minha segunda casa, que me possibilitou a realização de análises e o uso de materiais. Assim como ao NANOTEC, LABMAT, VITROCER, LCME, LCP,LPM, obrigada.

Ao Professor Márcio Celso Fredel, obrigada por sua atenção, disponibilidade e contribuição para a realização deste trabalho junto ao laboratório de materiais cerâmicos (CERMAT).

Ao PGMAT e a todos funcionários, meu muito obrigada.

Agradeço à agência de fomento CAPES pelo fornecimento da bolsa de estudos.

Aos membros da banca examinadora, obrigada por aceitarem o convite e participarem da defesa e discussão desta dissertação.

Por fim, a todos os meus amigos e familiares, que de forma direta ou indireta contribuíram na conclusão desta jornada.

A todos, muito obrigada!

RESUMO

Compósitos de matriz vítrea de borossilicato reforçados com alumina (CFG), (1-x)vidro + xAl_2O_3(x = 0 - 20% em volume) foram fabricados por sinterização convencional entre 800 e 850°C e pela técnica de queima rápida (*fast firing*) a temperaturas entre 850°C e 1000°C. Os efeitos do tamanho de partícula do vidro borossilicato e alumina, a taxa de aquecimento e o tempo de patamar sobre a composição de fases e a densificação foram investigados. Foi estudado o efeito da adição de Al_2O_3 na microestrutura, resistência à flexão, resistência à fratura, condutividade elétrica, e no coeficiente de expansão térmica. Al_2O_3 inibe parcialmente a formação de cristobalita e aumenta as propriedades mecânicas do vidro de borossilicato. Compósitos contendo 10% em volume de alumina fabricados por sinterização convencional mostraram densidade relativa de 97%, resistência à flexão de 175 MPa e resistência à fratura de 1,9 MPa.m$^{1/2}$. A observação do caminho de trinca e superfície de fratura mostraram que a deflexão, ponteamento e arrancamento pelos grãos de alumina foram os mecanismos responsáveis pelo aumento da tenacidade à fratura. Amostras fabricadas por queima rápida mostraram uma diminuição na resistência à flexão de ~50% que pode estar relacionada com a presença de microfissuras originadas pela transformação de $\beta \rightarrow \alpha$ da cristobalita durante o resfriamento rápido a partir da temperatura de sinterização. A dureza aumentou com a adição de alumina, assim como a constante dielétrica de 5.5 para vidro de borossilicato a 7.4 em compósitos contendo 10% em volume de alumina.

ABSTRACT

Alumina-filled borosilicate glass composites (1-x) glass + $x$$Al_2O_3$ (x=0, 5, 10vol.%) were fabricated by conventional sintering at 800 and 850^{o}C and by fast firing technique at temperatures between 850 and 1000^{o}C. The effect of the particle size of borosilicate glass and alumina, heating rate and holding time at maximum temperature on phase composition and densification was investigated. The effect of Al_2O_3 addition on the microstructure, flexural strength, fracture toughness, electrical conductivity, and thermal expansion coefficient is reported. Al_2O_3 hinders cristobalite formation and increases mechanical properties of borosilicate glass. Composites containing 10 vol% alumina fabricated by conventional sintering shown relative density of 98%, flexural strength of 175 MPa and fracture toughness of 1.9 MPa.m$^{1/2}$. Crack path and fracture surface observations shown that crack deflection, crack bridging and pull-out by alumina grains were the mechanisms responsible for the increase in fracture toughness. Samples fabricated by fast firing shown a decrease in flexural strength of ~50% when compared to conventional sintering that could be related to the presence of microcracks originated by β => α cristobalite transformation during rapid cooling from sintering temperature. In conventionally sintered samples hardness increased, from 4.75 in borosilicate glass to 5.6 GPa, and the dielectric constant from 5.5 to 6.5, in composites contain 5 vol.% alumina.

LIST OF FIGURES

Figure 1. Ternary solid-liquid-pore diagram showing different types of sintering.[25] 8
Figure 2. Two-particle model made of glass spheres. (x and r are, respectively, the radius of the neck and the sphere).[24] 9
Figure 3. Diagram of Scherer's model resembling the microstructure. l is the cell length and a is equivalent to the particle size. [33] 11
Figure 4. Compact with isolated pores of radius, a. [33] 12
Figure 5. (a) SEM micrographs of a polydispersed compact of an alumina-borosilicate glass.(b) Diagram of the Cluster model. [31] 13
Figure 6. Schematic illustration of viscous sintering of glass (G) with crystalline ceramic(C) composites.[36] 14
Figure 7. Effect of Al_2O_3 filler content on the relative density of the sintered composites in a borosilicate matrix.[23] 15
Figure 8. Internal crystallization in the formation of glass-ceramic from glass (a) nuclei formation, (b) crystal growth on nuclei, (c) glass-ceramic microstructure.[6] 17
Figure 9.Spherical cap model of heterogeneous nucleation.[2] 18
Figure 10. Free energy of spherical nuclei as function of its radius.[2] 18
Figure 11. Thermal expansion curves for polymorphic forms of silica.[6] 20
Figure 12. a) Tetragonal model of α-cristobalite;[6] b) Cristobalite crystals form in obsidian rock. 22
Figure 13. Plot of potential energy versus interatomic distance [49]. .. 23
Figure 14. Glass-network of SiO4 tetrahedrons. 24
Figure 15. Representation of alkali silicate glass network; where a) oxygens are bonded to one silicon, and Na+ is sharing one oxygen´s electron. b) Silicon tetrahedrally surrounded by four oxygens. 25
Figure 16. Volume expansivity of binary alkali silicates at indicated temperatures *vs*. composition. *ss* and *ls* refers to solid and liquid state, respectively[50]. 25
Figure 17. 3D representation of triangle structure of Boroxol ring $(B_3O_6)^{-5}$units changing to tetrahedral configuration with addition of Na_2O.[52] Triangles are indicated with black dots on the left hand side. Tetrahedron is indicated inside the continuous gray circle on the right hand side. ... 26
Figure 18. The fraction of boron atoms in fourfold coordination (N4) as function of concentration of alkalis oxides.[52] 27
Figure 19. Mean linear thermal expansion coefficients of alkali borate glasses as function of composition.[52] 28

Figure 20. Schematic representation of the percolation phenomena showing a square lattice being occupied by dots (a) shows parts of an square lattice; in (b) some squares are occupied with black dots; in (c) the clusters, groups of neighboring occupied squares, are encircled; (d) critical volume of inclusions, all the black dots are in contact.[54]...... 29
Figure 21. Number fraction of inclusions, showing where the percolation threshold begins, as function of R. [55] 30
Figure 22. Composite's microstructure scheme: matrix material filled by rigid particles.[58] 32
Figure 23. Residual stress schemes created on cooling a) tangential tensile stress on the matrix with a radial compressive stress on the particle and b) tangential compressive stress on the matrix with a radial tensile stress on the particles. 33
Figure 24. Process flow of a LTCC substrate.[60].............................. 35
Figure 25. Schematic representation of a three-points transverse bending test equipment.[49] 38
Figure 26. Top and cross-section views around Vickers indent as median cracks.[66].. 40
Figure 27. Schematic representation of a parallel plate capacitor.[70] 41
Figure 28. Scheme of a electric field of a single point A of charge of value *Q* [C] at a distance *R(m):*... 42
Figure 29. XRD analysis of ball-milled borosilicate glass.................. 44
Figure 30. Exposure controls section of hydrofluoric acid datasheet, and the protection apparatus used as underlines... 51
Figure 31. Fast firing procedure.. 52
Figure32. Particle size of borosilicate glass as function of milling time. 53
Figure 33. Particle size distribution of borosilicate glass after milled for 195 min. 54
Figure 34. SEM image of borosilicate glass particles after milling for 195 min. 55
Figure 35. Particle size distributions of as received Almatis Premium Alumina. 56
Figure 36. SEM image of as received aluminum oxide powder. 57
Figure 37. Dilatometric analyses of a borosilicate glass compact heated at indicated heating rate. 58
Figure 38. DSC analysis of borosilicate glass heated at 2°C/min. 59
Figure 39. Relative density of borosilicate glass samples after sintering at 800°C as function of particle size.. 60

Figure 40. XRD of sintered borosilicate glass at indicated particle sizes. 61
Figure 41. SEM image of borosilicate samples fabricated using powders of particle size as indicated, heated at 10°C/min to 800°C and sintered for 5 min. 62
Figure 42. Relative density of borosilicate glass samples sintered for 5 min at indicated temperatures using heating rates of 5, 10 and 15°C/min. 63
Figure 43. XRD of borosilicate glass, sintered at 800°C, using a holding time of 5 min and the indicated heating rates. 64
Figure 44. SEM images of borosilicate glass, sintered at 800°C, holding time of 5 min, varying the heating rate as indicated. Red circles show cristobalite crystals. 65
Figure 45. Relative density as function of sintering time for borosilicate glass powder compacts, heated at 15°C.min^{-1} up to indicated temperature. 66
Figure 46. Relative density as function of alumina content of borosilicate glass compacts heated at 15°C.min^{-1} up to 800°C and hold for 5 min, using alumina powders with particle size (D_{50}) as indicated. 67
Figure 47. Relative density as function of alumina content in borosilicate glass powder compacts heated at 15°C.min^{-1} up to indicated temperature and sintered during 5 min. 69
Figure 48. XRD of composites, sintered at 800°C, holding time of 5 min, varying alumina content as indicated. 70
Figure 49. SEM images of borosilicate glass and composites samples conventionally sintered at 800°C during 5 min and heated at 15°C/min. Alumina content as indicated. 71
Figure 50. Theoretical linear CTE of borosilicate glass and CFG composites containing 5 and 10 vol.% alumina, as function of cristobalite content between 25 and 300°C. ....**Error! Bookmark not defined.**
Figure 51. Relative density of borosilicate glass compacts as function of holding time after fast fired at indicated temperatures. 74
Figure 52. Relative density of alumina-filled borosilicate glass compacts as function of alumina content, fast fired at indicated holding time and temperatures. 75
Figure 53. SEM images of samples fast fired at 900°C for 3 min. 76
Figure 54. Flexural strength and Weibull distribution of borosilicate glass and CFG composites sintered at 800°C, heating rate of 15°C/min for 5 min. 78

Figure 55. Flexural strength and Weibull distribution of borosilicate glass and CFG composites fast fired at 900°C for 5 min. Composition as indicated. 79

Figure 56. XRD of samples conventional sintered during 5 min at 800°C, heating rate of 15°C/min and fast fired samples at 900°C for 5 min. Composition as indicated. 80

Figure 57. SEM images of samples tested mechanically conventionally sintered during 5 min at 800°C, heating rate of 15°C, and fast fired at 900°C for 5 min. 81

Figure 58.SEM images of crack path in borosilicate glass and CFG composites. 83

Figure 59.SEM image of conventional sintered alumina-filled borosilicate glass fabricated sintering time 5 min at 800°C, and heating rate of 15°C/min. 84

Figure 60. Fracture surface of conventionally sintered borosilicate glass and CFG composites, sintered during 5 min at 800°C, heating rate of 15°C/min. Alumina pull-out indicated by circles. 85

Figure 61. Vickers hardness of samples conventionally sintered during 5 min at 800°C, heating rate of 15°C/min, and fast fired at 900°C for 5 min. 86

Figure 62. Schematic representation of glass network containing Al^{3+} ions.[23] 88

Figure 63. Green tapes of mixtures of borosilicate glass with 5 vol.% alumina content. 89

Figure 64. Alumina-filled borosilicate glass tape containing 5 vol.% alumina, after sintered at 800°C for 5 min. 89

LIST OF TABLES

Table 1. Experimental data from literature of ceramic-filled borosilicate glass composites. 4
Table 2. Experimental data from literature of alumina-filled borosilicate glass composites 5
Table 3. Cristobalite structural data 20
Table 4. Physical properties of cristobalite 21
Table 5. Glass-ceramic substrates from different companies fabricated using LTCC technology. 36
Table 6. Typical chemical composition of borosilicate glass 43
Table 7. Physical data of commercial borosilicate glass (Pyrex®). 44
Table 8.Chemical composition of as received alumina (wt.%) 45
Table 9. Physical properties of as received alumina 45
Table 12. Dielectric constant at 1 MHz. 87

LIST OF ABBREVIATIONS

CFG	*Ceramic-filled glass*
CTE	*Coefficient of thermal expansion*
DSC	*Diffraction scanning calorimetry*
DIL	*Dilatometry*
HV	*Vickers hardness*
LTCC	*Low temperature co-fired ceramic*
LPS	*Liquid phase sintering*
NLPS	*Non-reactive liquid phase sintering*
SEM	*Scanning electron microscopy*
VGS	*Viscous glass sintering*
XRD	*X-ray diffraction*

INDEX

1. INTRODUCTION 1
1.1 Motivation 6
1.2 Objectives 6
1.2.1 General objective 6
1.2.2 Specific objectives 6
2. LITERATURE REVIEW 8
2.1 Sintering 8
2.1.1 Viscous flow sintering 9
2.1.2 Viscous sintering of glass-ceramic composites 13
2.2 Fast firing 15
2.3 Crystallization 17
2.4 Cristobalite 19
2.5 Thermal expansion 22
2.6 Percolation 29
2.7 Residual Stress 31
2.8 Definition of glass-ceramics and ceramic-filled glass 34
2.9 Low temperature co-fired ceramics 34
2.10 Characterization methods studied 37
2.10.1 Flexural strength 37
2.10.2 Fracture toughness 39
2.10.3 Dielectric constant 40
3. MATERIALS AND EXPERIMENTAL PROCEDURES 43
3.1 Materials 43
3.1.1 Borosilicate glass 43
3.1.2 Aluminum oxide 45

3.2 Powder characterization 45

3.2.1 Particle size and particle form 45

3.2.2 Powder density (true density) 46

3.3 Samples preparation 46

3.3.1 Uniaxial pressing 46

3.3.2 Sintering 46

3.3.3 Tape casting 47

3.4 Sample characterization 48

3.4.1 Thermal treatments 48

3.4.2 Bulk density 48

3.4.3 Determination of flexural strength 48

3.4.4 Determination of fracture toughness 49

3.4.5 Determination of Vickers Hardness (HV) 49

3.4.6 Determination of the coefficient of thermal expansion 49

3.4.7 Determination of the dielectric constant 50

3.4.8 X-ray diffraction 50

3.4.9 Scanning electron microscopy 50

4. Security 50

5. RESULTS AND DISCUSSION 53

5.1 Powder characterization 53

5.1.1 Borosilicate glass 53

5.1.2 Alumina 55

5.1.3 Powder density and green density of samples after pressing 57

5.2 Conventional sintering 58

5.2.1 Dilatometric and DSC analysis 58

5.2.2 Sintering 59

5.2.3 Conventional sintering of borosilicate glass and alumina compacts 66
5.2.4 Coefficient of thermal expansion (CTE) 72
5.2.5 Fast firing of borosilicate glass and alumina-filled borosilicate glass compacts 73
5.3 Flexural strength analysis 77
5.3.1 Conventional sintering 77
5.3.2 Flexural strength analysis of fast fired samples 79
5.4 Fracture toughness analysis 82
5.5 Vickers hardness analysis 86
5.6 Dielectric constant analysis 87
5.7 Tape casting of alumina-filled borosilicate mixtures 88
6. CONCLUSIONS 90
7. Appendix 1 91
7.1 Nucleation rate 91
7.2 Homogeneous nucleation rate 92
7.3 Heterogeneous nucleation rate 93
7.4 Crystal growth 94
8. REFERENCES 95

1. INTRODUCTION

Ceramic-filled glasses (CFG) are composites constituted of a vitreous matrix and ceramic filler. The different physical and chemical properties of the matrix and the filler when combined produce a composite with improved properties.[1] CFG when compared to pure glasses show an increase in mechanical resistance, microhardness, fracture toughness and voltage isolation.[2, 3]

The increase in mechanical resistance and fracture toughness is mainly related to the introduction of the reinforcements stronger (failure strength) than the matrices used. The resistance provided by reinforcements depends on their quantity and aspect ratio, e.g. whiskers, platelets and fibers form.

The enhancement of fracture toughness is due to matrix/reinforcement interrelation, which mainly causes cracks deviation, particles “bridges” and pull-outs with resultant fracture energy absorption. If the filler particles have a larger coefficient of thermal expansion than the matrix there is a development, during cooling, of a compressive stress in the matrix and a radial tensile stress close to the particle, so cracks are deflected away from the particles.[4] On contrary, if the filler particles have a lower coefficient of thermal expansion than the matrix, the matrix has more contraction therefore a compressive residual stress through the particles and a tensile stress on the matrix are generated.

Hardness is higher in ionic solids because of their crystalline structure, the ionic lattice. This holds the particles together with a strong polar bonding and allows breakage only along the polar edges of the lattice.[2] In a CFG composite the increase in microhardness is achieved by changing covalent bonds to ionic bonds due the interaction between matrix and filler.[2]

Borosilicate glasses show a higher voltage isolation compared to alumina.[1, 2] When compared to soda-lime glasses, borosilicate glasses present higher electrical stability. Soda-lime glasses contain alkaline ions such as Na^+ that under the effect of an electric field migrate, creating voids in the microstructure, decreasing the mechanical strength of the material.[5]

At temperatures >700°C, borosilicate glasses show the formation of cristobalite. Crystallization during the fabrication thermal cycle and thermal ageing results in a product exhibiting porosity and reduced strength due to the transformation during cooling from β to α cristobalite. The transformation is associated with changes in the volume of the unit cell.[6]

Al^{+3} ions act as a network former, and its presence inhibit the formation of cristobalite[7]. When alumina is used as filler in CFG [2, 8], the combination of borosilicate glass and alumina results in a material with a higher thermal stability in comparison to pure glass.[9]

Due to the low sintering temperature (<1000°C) CFG composites represent low-cost alternative to ceramics to be used as Low Temperature Co-fired Ceramics (LTCC) substrates in the microelectronic packaging industry.[10] Characteristics such as low CTE matching to silicon semiconductor material (3.10^{-6}/°C), low dielectric constant (5 at 1 MHz), sintering temperatures of around 800-850°C enabling co-firing with conductors such as gold and copper,[8, 11] make CFG composites an ideal substrate material.

CFG have been fabricated in the past using different types of borosilicate glass and ceramic fillers, e.g. lead borosilicate glass with alumina [3], soda-borosilicate glass with Si_3N_4 whiskers[12], borosilicate glass with SiC fibers[13], C-fibers[14], and zirconia fibers[15], (see Table 1). The sintering of borosilicate glass (Pyrex®)-alumina composites using particles and platelets as fillers has been reported [5-19], and a summary of related literature is presented in Table 2.

Table 1. Experimental data from literature of ceramic-filled borosilicate glass composites.

Glass Composition (wt.%)	Ceramic filler	Filler (vol.%)	Morphology	Particle size (μm)	Conformation Method	Sintering method	Sintering temperature (ºC)	Relative density (th.%)	Flexural strength (MPa)	CTE (10^{-6}.ºC^{-1})	Ref.
20PbO, $10B_2O_3$,, $67SiO_2$, $2A1_20_3$, $1Na_20$	Alumina	0-65	Particle	1-5	-	Hot pressing	800	73	122	-	[3]
80.3 SiO_2, 2.3 $A1_20_3$, $13.3B_2O_3$, $4Na_2O^*$	Si_3N_4	0-20	Whisker	5-200	Uniaxial Pressing	Conventional	1070	-	-	-	[12]
$79SiO_2$, $13B_2O_3$, $4Na_2O$, $2.5Al_2O_3$	SiC	0-60	Fiber	-	Tape casting	Conventional	1000	-	-	-	[13]
$79SiO_2$, $13B_2O_3$, $4Na_2O$, $2.5Al_2O_3^*$	Carbon	0-40	Fiber	-	-	Hot pressing	800-1300	94	1000	-	[14]
70–75 SiO_2, 20–25 $B_2O_3^*$	TiO_2	0-50	Particle	0.2	Uniaxial	Conventional	850-925	97		8	[16]
$60SiO_2.24B_2O_3$, $16Na_2O$	Zirconia	0-38	Fiber	-	Isostatic Pressing	Conventional	600-675	98	-	8.6	[15]
77PbO, $10B_2O_3$, $10SiO_2$, $2Al_2O_3$, $1P_2O_5$	Alumina	0-45	Particle	3	Uniaxial Pressing	Conventional	333-600	95	-	8.6	[17]
18PbO, 8.5 B_2O_3, $62SiO_2$, 8.5 CaO^*	Alumina	45	Particle	2.6	Tape casting	Conventional	550-925	98	-	8.1	[18]

*+ other alkaline oxides.

Table 2. Experimental data from literature of alumina-filled borosilicate glass composites

Alumina (vol.%)	Morphology	Particle size(μm)	Pressing method	Sintering method	Sintering temperature (ºC)	Holding time (min)	Relative density (th.%)	Flexural strength (MPa)	Fracture toughness (MPa.m$^{1/2}$)	Dielectric Constant (at 1MHz)	CTE (10^{-6}.ºC^{-1})	Ref.
0-10	Particle	0.6	Uniaxial	Conventional	900	240	85	-	-	-	-	[19]
0-10	Particle	3	Uniaxial	Conventional	750-900	480	-	-	-	-	-	[5]
0-30	Platelet	5-25	-	Hot pressing	650-800	-	99	150	1.9	-	-	[20]
0-50	Particle	100	Uniaxial	Conventional	600-1000	300	95	-	-	7.2	9.2	[21]
0-25	Particle	0.3-0.6	Uniaxial	Conventional	950	30	91	-	-	-	-	[22]
0-15	Platelet	2-5	Uniaxial	Conventional	800	60	97	122	1.4	-	-	[7]
0-25	Particle	2.5	Uniaxial	Conventional	800	180	92	-	-	5-7.2	5.9	[23]

1.1 Motivation

The present work was motivated to study borosilicate glass behavior during pressureless sintering, and to improve its mechanical properties such as flexural strength and fracture toughness, to fabricate a reliable substrate candidate, using LTCC technology, in microelectronic packaging.

1.2 Objectives

1.2.1 General objective

The main objective of this work refers to the development of guidelines to fabricate alumina-filled borosilicate glass composites investigating the relationship between processing parameters and final density.

1.2.2 Specific objectives

The specific objectives may be summarized as follow:

- Characterize the relationship between thermal treatment parameters such as sintering temperature, holding time and heating rate used, and the final density of compacts of pure borosilicate glass;

- Characterize the relationship between particles size of borosilicate glass powder and the density of compacts after sintering;

- Investigate the effect of thermal treatment parameters and powder particle size on glass crystallization;

- Produce CFG composites showing desired properties to use as substrates for electronic packaging such as high flexural strength, low dielectric constant and low coefficient of thermal expansion.

- Investigate the effect of fast firing on densification and final properties of the CFG composites.

- Characterize the CFG composites.

2. LITERATURE REVIEW

2.1 Sintering

Sintering is the process of firing and consolidating a body shaped from powder particles. [24] The driving force for sintering is the tendency to reduce the free energy of the system.[2, 25, 26] As shown in Fig. 1, considering the solid-liquid-pore content sintering processes can be divided into four categories:

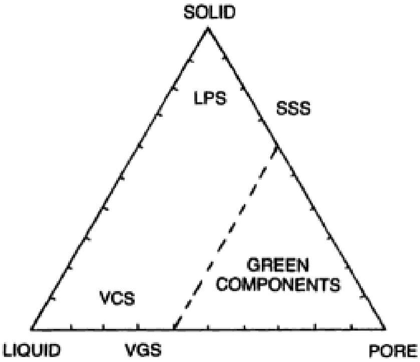

Figure 1. Ternary solid-liquid-pore diagram showing different types of sintering.[25]

- Solid state sintering (SSS), which involves only solid and pores and so is covered by the right-hand edge of the figure; [27]

- Liquid phase sintering (LPS), which involves all three components but is concentrated at the solid apex since most material is solid (< 20% liquid); [28]

- Viscous glass sintering (VGS), also termed *viscous flow* which is the glass powders densifying mechanism present in glazing and enameling. This involves liquid (molten glass) and pores, and; [27, 29]

- Viscous composite sintering (VCS) or vitrification, where liquid content is >20% and is the region relevant to sinter whiteware such as porcelain. [25, 27]

2.1.1 Viscous flow sintering

Viscous sintering occurs when a viscous glass or liquid present at the sintering temperature flows under the action of the capillary force filling up the porosity of the body. [24, 30] Fig. 2 shows an example of the sintering of two glass particles by viscous flow. [24]

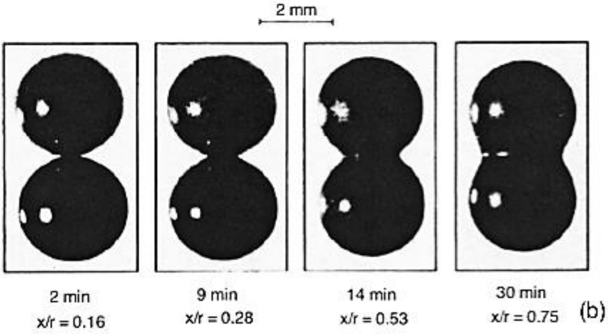

Figure 2. Two-particle model made of glass spheres. (x and r are, respectively, the radius of the neck and the sphere).[24]

Although the path by which matter flows is still under discussion,[29, 30] three models have been proposed to explain the different stages during viscous flow sintering: an initial (Frenkel's model), an intermediate (Scherer's model) and a final (Mackenzie–Shuttleworth's model). [24, 31]

Frenkel's model (F) of viscous sintering describes the early stages of sintering of spherical and mono dispersed particles, and allow to calculate the shrinkage rate of two equal particles whose centers approximate each other. The energy released by the decrease of surface area is used for viscous flow, which is responsible for the mass transport that produces densification.[29] The rate of initial neck growth (see equation 1) increases with the contact radius, x, and is proportional to the square root of time, t. [24, 31]

$$\frac{x}{r} = \left(\frac{3\gamma}{2\eta r}\right)^{1/2} t^{1/2} \tag{1}$$

where γ is the surface energy and η is the viscosity of the material.

The macroscopic result of particles whose centers approximate each other is a linear shrinkage, y, of the powder compact, and can be calculated using equation 2, [24]

$$y \approx \frac{x^2}{4r} \tag{2}$$

the relative change in length, y/r, is [24]

$$\frac{y}{r} = \frac{3\gamma}{8\eta r} t \tag{3}$$

Thus the initial rate of shrinkage is directly proportional to time (t) and to the surface tension (γ) and inversely proportional to the viscosity (η) and particle size (*r*). [24, 32]

For the intermediate stage of viscous sintering, G. W. Scherer (S) proposed a model of basic cells which are a cubic array of intersecting cylinders (see Fig. 3). The cylinders stand for strings of particles. In this model, particles are aligned along the borders of a cubic structural unit, and each particle has a small number of neighbors and, hence, a small number of contacts. [29]

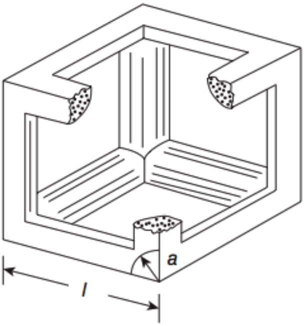

Figure 3. Diagram of Scherer’s model resembling the microstructure. l is the cell length and a is equivalent to the particle size. [33]

For this model, Scherer derived the densification rate ($\dot{\boldsymbol{\varepsilon}}_{\boldsymbol{f}}$) given by [33]

$$\dot{\boldsymbol{\varepsilon}}_{\boldsymbol{f}} = -\left(\frac{\gamma n^{1/3}}{\eta}\right)\frac{\pi-4\sqrt{2}x}{x^{1/3}\left(3\pi-8\sqrt{2}x\right)^{2/3}} \tag{4}$$

where the variable x is correlated to the relative density ρ through the follow equation.

$$\rho = 3\pi x^2 - 8\sqrt{2}x^3 \tag{5}$$

n is the number of pores per unit volume, and using the geometric model shown in Fig. 3, in terms of geometric parameters and green density :

$$\boldsymbol{n^{1/3}} = \frac{1}{l_0 {\rho_0}^{1/3}} \tag{6}$$

where

$$\boldsymbol{l_0} = \frac{\sqrt{\pi d_0}}{2(1-2x_0)^2} \tag{7}$$

and x_0 is the root of equation 7 considering that $\rho = \rho_0$, where ρ_0 is the initial relative density and d_0 is the initial particle diameter.

The model developed by J. K. Mackenzie and R. Shuttleworth

(M–S) describes the final stage of viscous sintering, when the pores are spherical and isolated in the glass, as shown in Fig. 4. [31, 34]

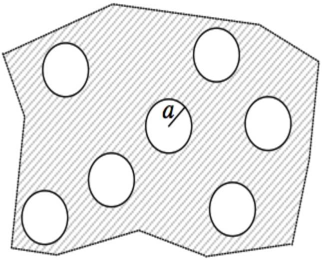

Figure 4. Compact with isolated pores of radius, a. [33]

In terms of that structure, the Mackenzie and Shuttleworth model gives the following densification rate:[29]

$$\frac{d\rho}{dt} = \frac{3\gamma}{2a_0\eta}(1-\rho) \qquad (8)$$

where a_0 is the initial pore radius.

Based on the fact that small particles preferentially cluster in the open spaces left by larger particles, and sinter faster, the Clusters model was further developed.[29] Each of these clusters sintered individually, passing through the stages proposed by Frenkel and Mackenzie-Shuttleworth.

The model considers the sample's shrinkage as the sum of the partial shrinkage of clusters, each consisting of equally sized particles and showing an independent F or M–S behavior. Fig. 5 shows that the F and M–S behavior may occur simultaneously in a sample having a particle-size distribution. [31]

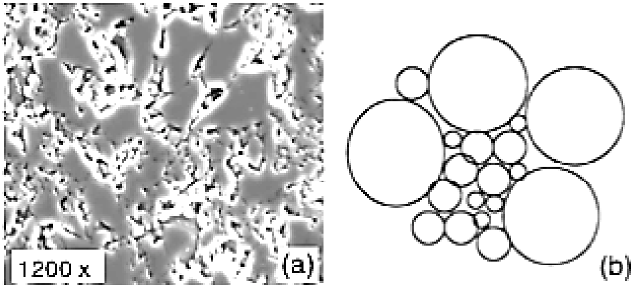

Figure 5. (a) SEM micrographs of a polydispersed compact of an alumina-borosilicate glass.(b) Diagram of the Cluster model. [31]

For a polydispersed compact with volume fraction v_r of particles of radius *r*, the following expression holds true for the densification kinetics at a given temperature: [29]

$$\boldsymbol{\rho(t)} = \frac{\sum_r [\boldsymbol{\rho_F(r,t)\xi_r\theta_{\mathrm{F}}(t_{0.8}}-t)+\rho_{\mathrm{M-S}}(r,t)\theta_{\mathrm{M-S}}(t-t_{0.8})]\nu_r}{\sum_r [\nu_r\xi_r\theta_{\mathrm{F}}(t_{0.8}-t)+\theta_{\mathrm{M-S}}(t-t_{0.8})]} \qquad (9)$$

Equation 9 sums up the relative density $\rho(r, t)$ for each particle size, *r*, as a function of time, *t*. During the Frenkel´s stage of sintering, the $\rho(r, t) = \rho_F(r, t) < 0.8$ condition is met and $\rho_F(r, t)$ is calculated using the Frenkel´s equation. Later, $\rho(r, t) = \rho_{M\text{-}S}(r, t) > 0.8$, and $\rho_{M\text{-}S}(r, t)$ is calculated by the M-S worth model. For each cluster, the passage from the Frenkel regime to the M-S regime is performed using the step functions $\theta_F(t_{0.8} - t)$ and $\theta_{M\text{-}S}(t - t_{0.8,})$, whose values alternate between 1 and 0 at $t = t_{0.8}$ when $\rho_F(r, t) = 0.8$ is reached. Thus, $\theta_F(t_{0.8} - t) = 1$ and $\theta_{M\text{-}S}(t - t_{0.8}) = 0$ for $t < t_{0.8}$, $\theta_F(t_{0.8} - t) = 0$ and $\theta_{M\text{-}S}(t - t_{0.8}) = 1$ for $t > t_{0.8}$. ξr is the neck-forming ability of each particle, which can be calculated from the particle-size distribution and $\xi_r = 1/r^C$, where *c* is a constant that depends on the particle-size distribution.[31, 32]

2.1.2 Viscous sintering of glass-ceramic composites

Composite materials of vitreous matrix loaded with ceramics (CFG) densify by a three stage process described as “non-reactive liquid phase sintering” (NLPS).[35] As shown in Fig. 6 densification is a combination of glass redistribution, grain rearrangement and viscous flow.

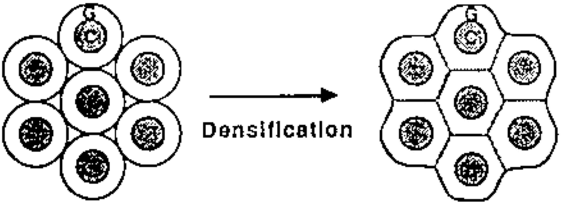

Figure 6. Schematic illustration of viscous sintering of glass (G) with crystalline ceramic(C) composites.[36]

The densification during NLPS depends on the ceramic filler concentration , the viscosity of the matrix, and the viscosity of the CFG composite[37]. Composite densification may be hindered when the concentration of “non-sinterable” inclusions is sufficient high to form a connected ceramic particulate network. [36] Densification rate usually decrease as the volume fraction of the filler increases. The effect of Al_2O_3 content on the relative density (ρ_r) is illustrated in Fig.7. The relative density of the composites decreases for volume fractions of filler higher than 5%.[23]

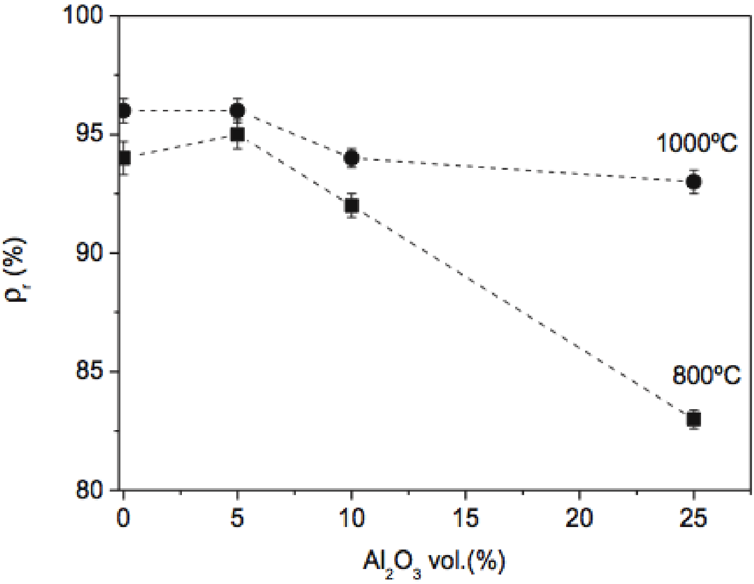

Figure 7. Effect of Al_2O_3 filler content on the relative density of the sintered composites in a borosilicate matrix.[23]

2.2 Fast firing

In conventional firing of ceramic materials a constant heating rate, generally ≤ 15°C/min, is used until reaching a maximum sintering temperature (T_{max}) and a holding time at T_{max} until obtained the required densification level is obtained. [52-54]During heating, the temperature of the surface changes continuously while the temperature within the sample changes according to the thermal diffusivity (TD). [41, 42] The thermal diffusivity is a thermal inertia that indicate show how fast the heat diffuses through the material. The higher the thermal diffusivity of the material the greater the rate at which heat is transported from the surface to the center of the powder compact during heating.

A high thermal gradient ensures greater heat diffusion within the compact. For a specific material the gradient depends on the rate of heat input at the surface. Faster heating rates generate higher thermal gradient, and rapid densification. [39] During the heating up process in a conventional furnace, the rate of surface heating is governed primarily by the rate of heat transfer from the furnace to the body. Convection provides the major contribution to the total heat transfer at lower temperatures, and radiation is the typically controlling factor at high sintering temperatures. Radiation quickly heats the surface of the green compact, and then the heat diffuses toward the center of the body. [42]

The fastest heating rate possible to be obtained using conventional heating is accomplished by radiation, when a powder compact is introduced into a preheated intermittent furnace at sintering temperature or into a sintering zone in a continuous furnace. This procedure has been used in the past, in combination with a short (≤ 10 min) or even no dwell time, and it is known as fast firing, [43, 44] and has been shown to be effective for achieving high density and fine grain size in several ceramics, for example $Al_2O_3$and $BaTiO_3$.[45] When a powder compact is introduced into the preheated furnace at Tmax, the densification mechanisms, such as grain boundary and lattice diffusion, are favored. [46, 47] The short residence time of the compact in the furnace at Tmax, hinders grain growth increasing the driving force for sintering and densification occurs in an abnormally high rate. [46, 47]

These high densification rates observed during fast firing could also be related to a change in the internal structure of the powder compact. [42] The presence of high thermal gradients within the compact during fast firing are responsible for the formation of a densification front moving from the outer surface toward the center of the sample. [42] The formation of a dense outer layer controls the flux of heat to the interior of the compact increasing the rate at which heat diffuses from the outer surface to the center of the body and the amount of energy available for sintering. [41] The velocity of the densification front moving from the outer surface toward the center of the compact determines the time necessary to achieve full densification. [48]As long as the rate of heat transfer is enough to sustain the advance of the sintering front, no differential densification occurs. [42]

2.3 Crystallization

Crystallization is the process of formation of solid crystals precipitating from a supersaturated medium such as a solution, a melt or a gas. In glasses there are two types of crystallization: surface and internal. Surface crystallization begins at the surface of a material and progresses into the volume. Internal crystallization, occurs when crystals form in the bulk of the precipitating medium.[18] The crystallization process consists of two major events: nucleation and crystal growth.[6] Fig. 8 shows an example of internal crystallization in the formation of glass-ceramic from glass.

In the nucleation process, a nuclei grow into crystals through mass diffusion, and the driving force for it is the change in free energy between the supersaturated medium and crystal. There are two types of nucleation: homogeneous and heterogeneous. In homogeneous nucleation, the nuclei has the same composition of its precursor[2]. Nuclei are formed as molecules constantly colliding with the surrounding molecules and start to gather into clusters [6] forming particles smaller than a stable nucleus named embryos. On further growth however, once embryo reach a critical size or radius, r*, with a respective free energy of formation of an embryo of critical size, ΔG^*, it remains growing by material deposition. That leads to a lower free energy and a stable system, until the formation of crystals[2].

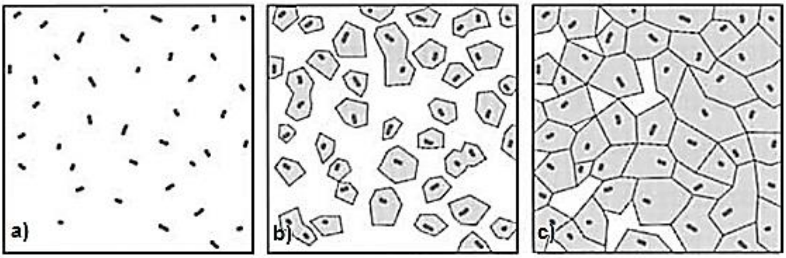

Figure 8. Internal crystallization in the formation of glass-ceramic from glass (a) nuclei formation, (b) crystal growth on nuclei, (c) glass-ceramic microstructure.[6]

In heterogeneous nucleation, foreign particles added to the melt or structural imperfections such as bubbles and die walls, named substrates, act as nuclei, lowering the thermodynamic barrier to nucleation[6]. The lower the wetting contact angle between the supersaturated melt and the substrate, θ, the higher the possibility to the substrate act as nuclei (see Fig. 9), as the free energy decreases with decreasing contact angle.

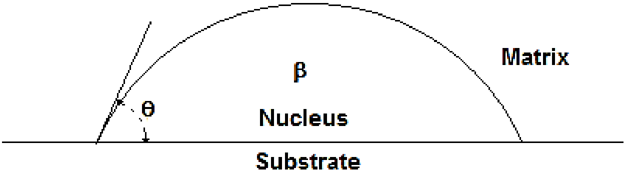

Figure 9. Spherical cap model of heterogeneous nucleation.[2]

Fig. 10 shows the change in the free energy of a spherical nucleus as function of its radius for an embryo of a critical size, for homogeneous, ΔG^*, and heterogeneous nucleation, ΔG^*_{het}.

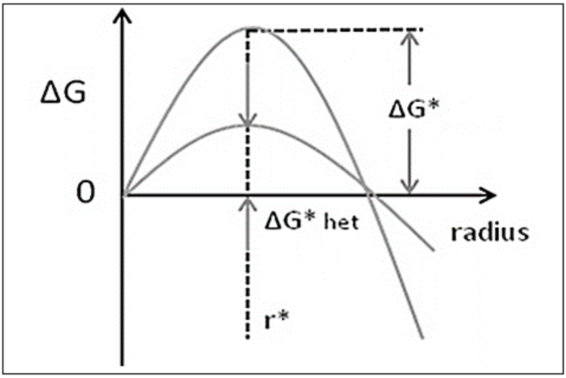

Figure 10. Free energy of spherical nuclei as function of its radius.[2]

The critical radius, *r**, is the same for both homogeneous and heterogeneous nucleation. However, the free energy is smaller for heterogeneous nucleation.[2]

For further crystallization kinetics concepts such as nucleation rate, homogeneous and heterogeneous nucleation rate and crystal growth, see Appendix 1.

2.4 Cristobalite

The silica polymorph forms are quartz, tridymite, and cristobalite. Cristobalite has an anisotropic expansion behavior and is the high temperature crystalline form of silica. Cristobalite undergoes a rapid, reversible inversion from a high-temperature cubic structure, β-cristobalite to low-temperature tetragonal structureα-cristobalite, at ~215°C, during cooling.[6]

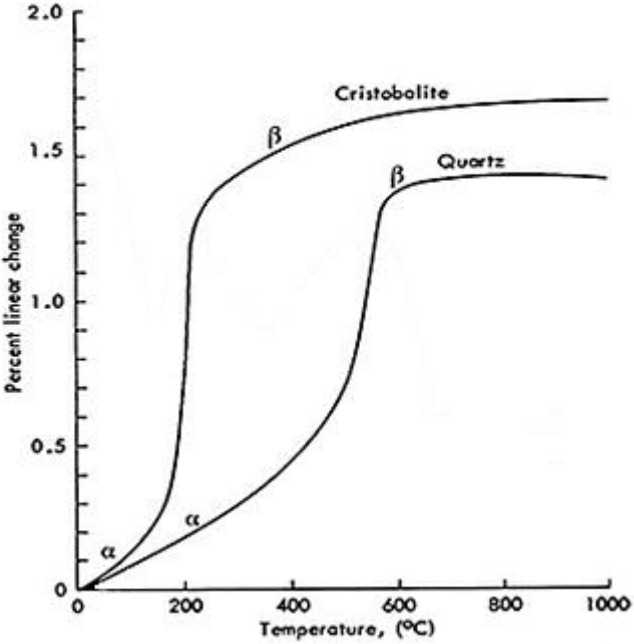

Figure 11. Thermal expansion curves for polymorphic forms of silica.[6]

Table 3 shows the changes in structural data for both types, α and β cristobalite, the changes in their unit cells, and consequently causing a large change in thermal expansion. The a- and c-axis of α-cristobalite increase rapidly at rates of 9.3×10^{-5} and 3.5×10^{-5}, Å°C^{-1}, respectively; whereas in β-cristobalite, a-axis expands at only 2.1×10^{-5}Å°C^{-1}. This behavior translates into very large, spontaneous strains of -1% along a-axis and -2.2% along c-axis during inversion, creating microcracks during cooling.[6]

Table 3. Cristobalite structural data

Structural Data for Cristobalite		
Unit Cell	β-Cristobalite	α-Cristobalite
a (Å)	7.1	4.9
c (Å)	--	6.9
V (Å^3)	361	171

Some physical properties of cristobalite are shown in Table 4. Fig. 12 shows an idealized (a) model of α-cristobalite, corner-bonded SiO_4 tetrahedral. And (b) shows its crystal form crystallized in an obsidian rock matrix.[6]

Table 4. Physical properties of cristobalite

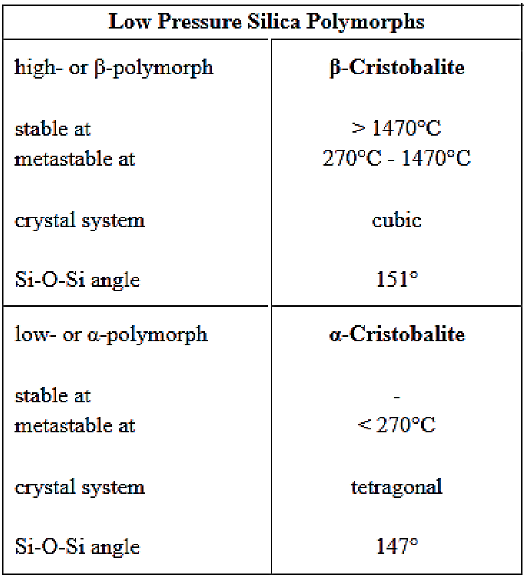

Low Pressure Silica Polymorphs	
high- or β-polymorph	**β-Cristobalite**
stable at	> 1470°C
metastable at	270°C - 1470°C
crystal system	cubic
Si-O-Si angle	151°
low- or α-polymorph	**α-Cristobalite**
stable at	-
metastable at	< 270°C
crystal system	tetragonal
Si-O-Si angle	147°

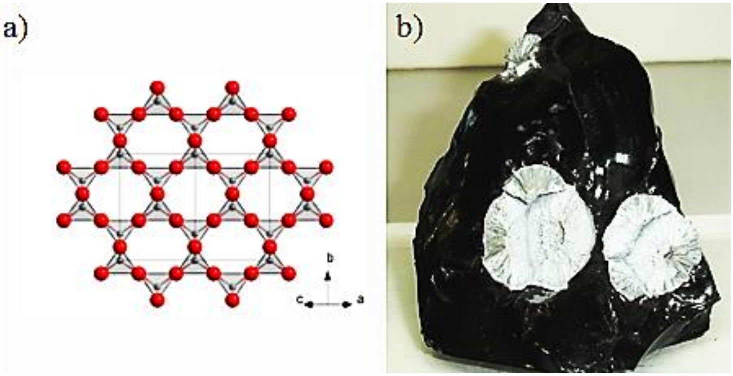

Figure 12. a) Tetragonal model of α-cristobalite;[6] b) Cristobalite crystals form in obsidian rock.

2.4.1 Cristobalite inhibition in borosilicate matrix by alumina particles

During the sintering of compacts, a strong coupling reaction between alkali ions from borosilicate glass (BSG) and $Al^{+3}$from alumina occurs, thus causing a diversion in the transport of alkali ions from BSG to alumina, and Al^{+3} ions to the matrix. Due to of this strong coupling between alkali and Al^{+3} ions, the resulting reaction layer around alumina is formed far more rapidly than that of cristobalite formation which is thus its rate-controlling step.[5, 7]

2.5 Thermal expansion

Changes in temperature affect the dimensions of a body. Thermal expansion is a consequence of an increase in the average distance between the atoms. The interatomic distance depends on the potential energy of the system, which increases with temperature. As shows Fig. 13, the potential-energy-versus-interatomic-spacing curve for a solid material has the form of a potential energy trough. The value r_0 corresponds to the trough minimum, i.e., the interatomic distance of equilibrium at 0 K. Heating to higher temperatures increases the vibrational energy from E_1

to E_2 to …E_n, and the atomic vibrational amplitudes from r_1 to r_2 to …r_n. The vibrational average amplitude corresponds to the trough width at each temperature, and is represented by its mean position.[49]

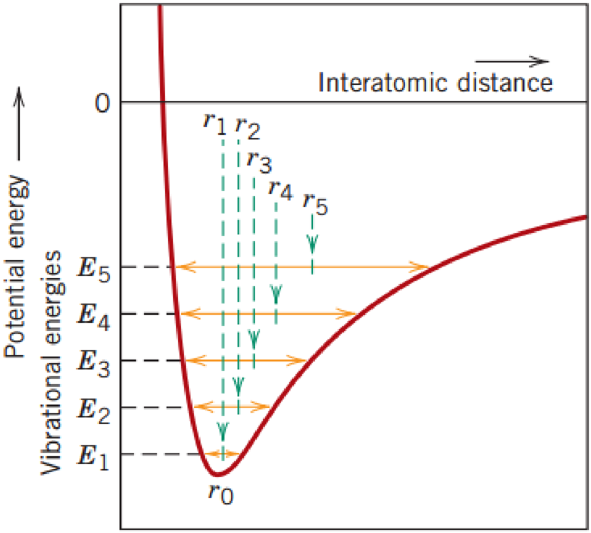

Figure 13. Plot of potential energy versus interatomic distance [49].

The expansion with increasing temperature is due to the asymmetric curve form of the potential energy trough, rather than the distance of the atomic vibrational amplitude. If the potential energy curve were symmetric, there would be no net change in interatomic separation and, consequently, no thermal expansion could be observed. The potential energy trough depends on the bonding strength, i.e., the energy required to separate two atoms. The greater the atomic bonding energy, the deeper and narrower its potential energy trough.[49]

The CTE of a material quantifies how dimensions change with temperature measuring the fractional change in size per degree. CTE is related to the molecules bond strength, which in turn depends on the ionic radii size. The larger the radii atomic the *weaker* the bond strength. The greater the distance between nuclei and electrons, the weaker the attraction between them and the higher the CTE. Strong ionic bonding forces found in ceramics imply in low values of CTE, which range between $0.5x10^{-6}$ and $15x10^{-6}$/°C.[49] For metals, due to their metallic bonds, interatomic forces are weaker than ceramics and consequently have a higher CTE, most ranging from $10x10^{-6}$to $25x10^{-6}$/ºC. For inorganic glasses, which have ionic and covalent bonds, the coefficient of thermal expansion range between $3.0x10^{-6}$ and $10x10^{-6}$/ºC.

The addition of alkali oxides on glasses promote oxygen bond break affecting the thermal expansion. Pure silica glass at room temperature is a three-dimensional random network of edge-linked SiO_4 tetrahedrons bonded in different angles. As shown in Fig. 14, silicon is tetrahedrally surrounded by four oxygens and each oxygen is bonded to two silicons. In an alkali silicate glass silicon is tetrahedrally surrounded by four oxygens but some of the oxygens are only bonded to one silicon as shown in Fig. 15.[50] The alkali ions are held weakly in the silicon-oxygen network, compensating the negative charges of the broken bonds created by the addition of the alkalis oxides. Consequently the addition increases the CTE of glasses due the formation of weaker bonds. As shown in Fig. 16, when alkaline oxides are added to silicate glasses, the value of its coefficient of thermal expansion follows the order of the radii size of the added cation: K>Na>Li.

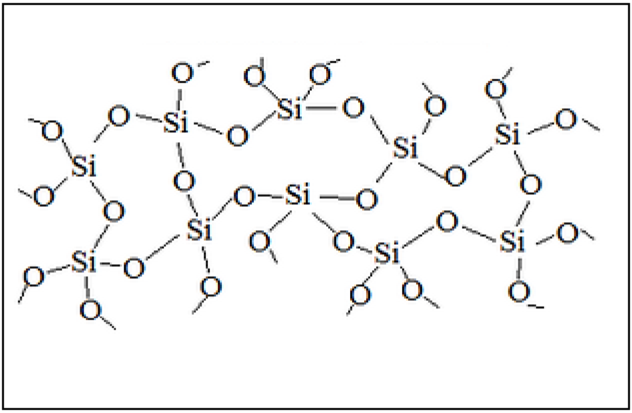

Figure 14. Glass-network of SiO_4 tetrahedrons.

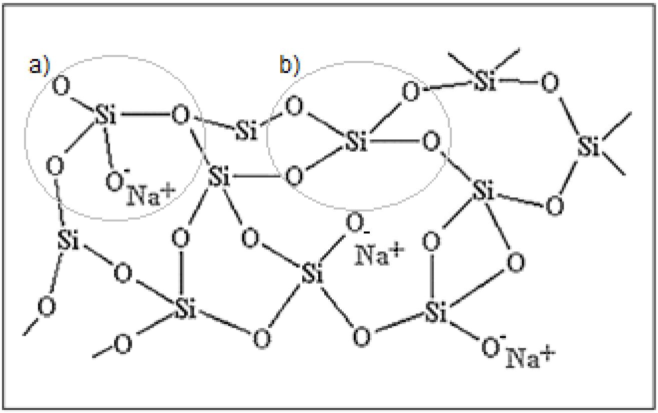

Figure 15. Representation of alkali silicate glass network; where a) oxygens are bonded to one silicon, and Na^+ is sharing one oxygen´s electron. b) Silicon tetrahedrally surrounded by four oxygens.

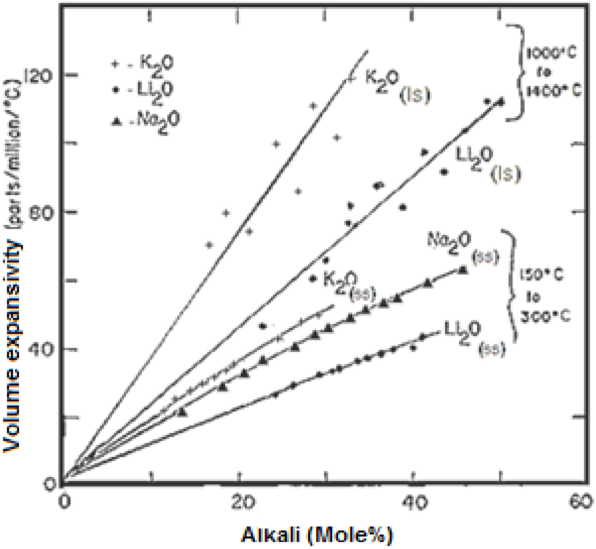

Figure 16. Volume expansivity of binary alkali silicates at indicated temperatures *vs*. composition. *ss* and *ls* refers to solid and liquid state, respectively [50].

The CTE of borate glasses shows a different behavior than alkali silicates glasses when alkaline oxides are added. Borons change the number of surrounding atoms as a result of oxygen added from alkaline molecules to the vitreous network [2]. The glass bonds become stronger when all the oxygens stemmed from alkalis are bonded and consequently the CTE decreases; the network composed only of B_2O_3 where each boron has coordination 3, and a planar triangle configuration units $(BO_3)^{-3}$ are connected tridimensionally by oxygen bridges. The resulting arrangement is known as Boroxol ring $(B_3O_6)^{-3}$. [51] With the continuous addition of alkali ions the coordination number changes to 4, creating a tetrahedral form. Each oxygen stemmed from alkalis oxide, breaks a B-O-B bond, producing two non-bridging oxygen, and the formation of two boron-oxygen tetrahedral consume the additional oxygen originated from the alkali oxide. The negative charges generated, are compensated by the alkalis ions and the tetrahedral $(BO_4)^{-5}$, as shows Fig. 17 [52] acts like an anion associated with a cation. The addition of alkali ions results in a progressive *strengthening* of the network and then the CTE decreases.

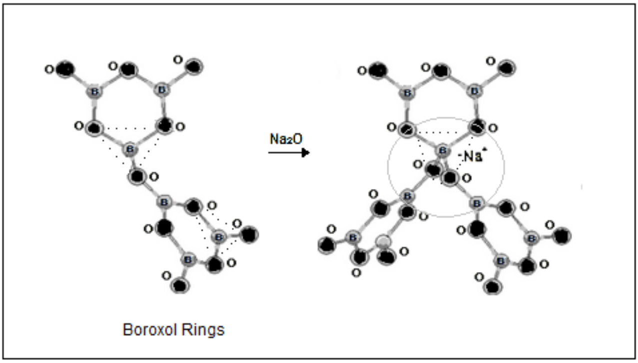

Figure 17. 3D representation of triangle structure of Boroxol ring $(B_3O_6)^{-5}$units changing to tetrahedral configuration with addition of Na_2O.[52] Triangles are indicated with black dots on the left hand side. Tetrahedron is indicated inside the continuous gray circle on the right hand side.

The addition of alkalis ions up to 35 mol% to borates glasses results in a continuous reinforcement of the network. At higher concentrations boron starts to change its coordination number from 4-fold to 3-fold. Without the formation of non-bridging oxygen the triangles configuration begins to form again, and the tetrahedrons starts to extinguish up to complete elimination around 65-75 mol% of alkalis addition as shows Fig.18.

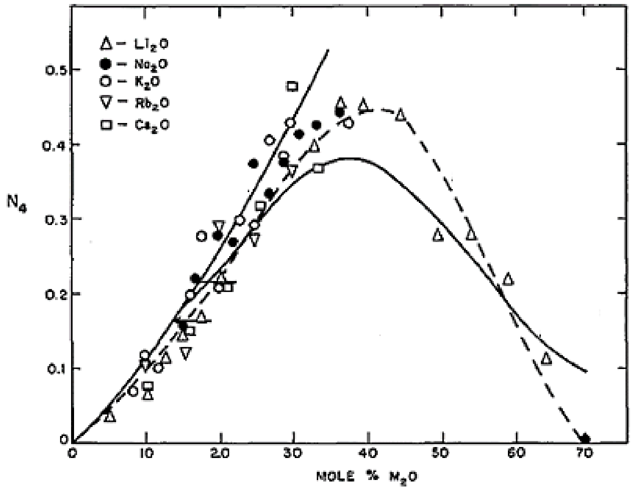

Figure 18. The fraction of boron atoms in fourfold coordination (N4) as function of concentration of alkalis oxides. [52]

In Fig. 19 the resulting linear thermal expansion coefficients of alkali borate glasses as function of alkalis composition, is shown. The decrease in the CTE and a graduate increase above around 35 mol%, is originated in the resumption of triangle configuration.

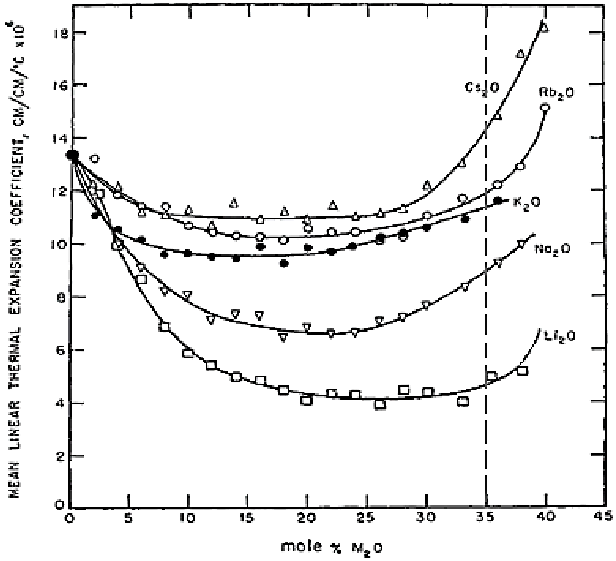

Figure 19. Mean linear thermal expansion coefficients of alkali borate glasses as function of composition. [52]

The thermal expansion of polycrystalline materials is a consequence of the relative composition and CTE of each phase, and the microstructure (porosity, microcracks, anisotropic crystal structure) [51]. The CTE is the sum of the product of the CTE´s of each phase by its volumetric fraction [2]. In a crack-free composite CTE can be calculated if it´s assumed that the expansion of each grain is the same as the overall expansion [2], for a composite constituted of i-phases CTE can be calculated using the equation developed by Turner:

$$\alpha_m = \frac{\sum \alpha_i . v_i . K_i}{\sum v_i . K_i} \tag{10}$$

where v_i and K_i are respectively the volume fraction and the bulk modulus, which is the resistance to uniform compression, of the i-phase. [2]

2.6 Percolation

Percolation is the formation of long-range connectivity in a random particulate system. In a binary system, at a critical concentration inclusions start to contact with each other and form an extended rigid network.

The percolation threshold is the critical value of the occupation probability *p*, such that connectivity (*percolation*) first occurs.[53] The percolation threshold refers to simplified lattice models in random systems or networks and the nature of the connectivity in them. Considering a large d-dimensional densely-packed powder compact formed by random mixing of convex-shaped rigid (inclusions) and non-rigid (matrix) particles, at the percolation threshold the rigid particles form a large connected network (or cluster). Considering the interaction of spherical particles, the percolation threshold is reached when the volume fraction of particles is 16 vol.%, and at a critical volume of inclusions of 64 vol.% all the inclusions are connected into a network (probability p=1).[53, 54]

Fig. 20 illustrates schematically the percolation phenomena. The occupation of a lattice of *N* squares, *N* being a very large number, and *p* the probability of a square lattice being occupied by a dot; then $p.N$ defines the number of squares occupied, and $(1-p).N$ the number of squares empty.[26]

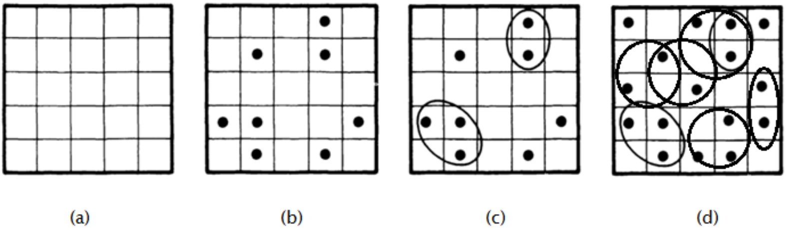

Figure 20. Schematic representation of the percolation phenomena showing a square lattice being occupied by dots (a) shows parts of an square lattice; in (b) some squares are occupied with black dots; in (c) the clusters, groups of

neighboring occupied squares, are encircled; (d) critical volume of inclusions, all the black dots are in contact.[54]

Considering spherical particles and no variation of particle size of both the matrix and inclusions, some models have been proposed to identify the critical fraction of inclusions where the percolation begins[55]. As shown in equation 11 for the Bouvard and Lange´s model, the percolation threshold is determined by R, which is the size ratio between R_m, the radius of matrix particles, and R_i the radius of the inclusion particles,

$$n_i = \frac{f_i}{f_i + \frac{(1-f_i)}{R^3}} \tag{11}$$

where n_i is the number of inclusions, f_i the volume fraction of inclusions, and R the size ratio. Fig.21 shows the dependence of the percolation threshold with R. [55]

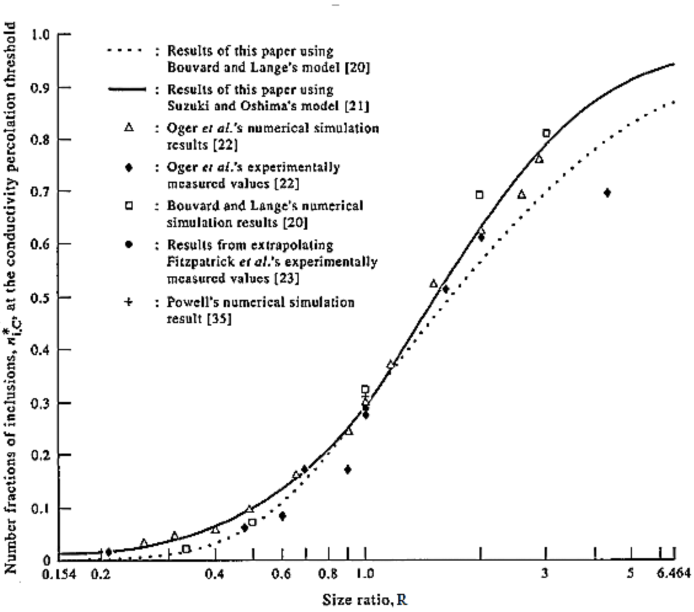

Figure 21. Number fraction of inclusions, showing where the percolation threshold begins, as function of R. [55]

The sintering of a composite where the inclusion concentration is higher than the percolation threshold decreases due to the formation of a rigid network. The formation of a continuous network of inclusions reduces the sintering, inhibiting the densification. The increased stiffness due to rigid contacts between particles, retards sintering, and if the structure is completely rigid, sintering not further progress.[45]

2.7 Residual Stress

In glass matrix composites reinforced by rigid particles, the presence of a secondary phase generates residual stress due to the difference in thermal expansion coefficients and the magnitude of this stress is dependent on the mismatch in elastic modulus among phases. Also microcracking in brittle materials generally results from large localized residual stresses that develop from either thermal contraction anisotropy or a phase transformation.[56]

The microstructure of such composite comprises a matrix material filled by rigid inclusions, as shows Fig. 22. When the coefficient of thermal expansion of the dispersed phase is larger than that of the matrix material, thermal residual stress will become the dominant toughening mechanism in ceramic materials.[57]

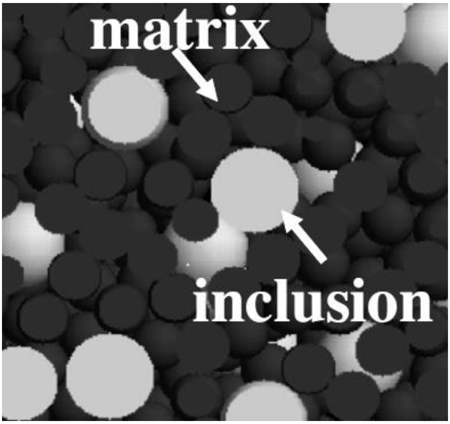

Figure 22. Composite's microstructure scheme: matrix material filled by rigid particles.[58]

On the reinforcement of such composites, the improvement in mechanical properties is mainly related to fracture toughness due to crack deflection.[7] The direction of the extension of a crack may change when it meets an obstacle such as a second phase particle. [4]

The enhancement of fracture toughness is due to matrix/reinforcement interrelation, which mainly causes cracks deviation, particles "bridges" and pull-outs with resultant fracture energy absorption. If the filler particles have a larger coefficient of thermal expansion than the matrix, there is a development, during cooling, of a tangential compressive stress in the matrix and a radial tensile stress close to the particle, so cracks are deflected away from the particles.[59] A crack propagates perpendicular to the tensile axis and parallel to the compressive stress, which means that the residual stress field may also deflect the crack.[4] Fig. 23 shows both cases.

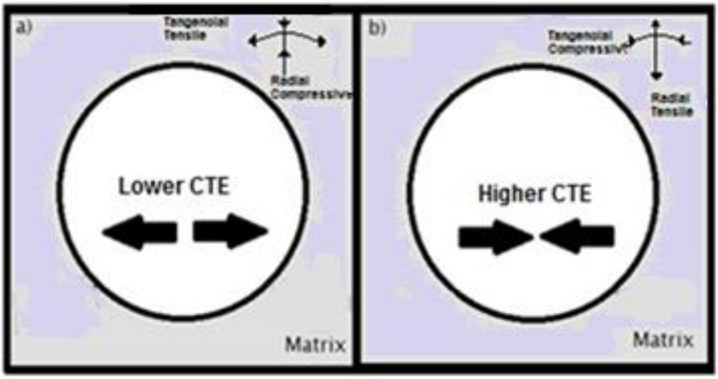

Figure 23. Residual stress schemes created on cooling a) tangential tensile stress on the matrix with a radial compressive stress on the particle and b) tangential compressive stress on the matrix with a radial tensile stress on the particles.

A particle having a thermal expansion coefficient higher than the matrix has around itself a radial tension and hoop compression. Such a stress field produced by the particle in the plane of a crack may deflect the crack and force it to travel around the particle. Due to this deviation in direction, the crack travels a longer path and the stress intensity at the crack tip is reduced since the plane of the crack is no longer perpendicular to the tensile stress. [4]

A misfit between the coefficients of thermal expansion introduces a stress field in the matrix and can also produce microcracks when the residual stress is larger than the mechanical strength: If the filler particles have a lower coefficient of thermal expansion than the matrix, the matrix has more contraction therefore a compressive residual stress through the particles and a tensile stress on the matrix are generated.

On toughening, the main crack may be deflected or branch in the presence of microcracks, reducing the stress intensity at the crack tip and, consequently, increasing toughness. Conversely, excessive microcracks can also lead to a decrease in fracture toughness and fracture strength.[4]

2.8 Definition of glass-ceramics and ceramic-filled glass

Glass-ceramics are ceramic materials formed through the controlled nucleation and crystallization of glass. Glasses are melted, shaped, and then thermally converted into a predominantly crystalline ceramic. The basis of controlled internal crystallization lies on an efficient nucleation that allows the development of a pore-free and crackless glass-ceramic containing small and randomly oriented grains, generally. Glass-ceramics have the fabrication advantage of glass as well as properties of ceramics such as mechanical resistance, voltage isolation and biocompatibility.[6]

CFG are ceramic materials formed through an addition of a crystalline second phase in a glass matrix, usually used as reinforcement, allowing the material to combine the different physical and chemical properties of the matrix and the filler producing a composite with improved properties.[1] CFG when compared to pure glasses show an increase in mechanical resistance, microhardness, fracture toughness and voltage isolation.

2.9 Low temperature co-fired ceramics

LTCC is a technology used to produce substrates for multilayer circuits from through the co-firing of stacks of individual tapes of ceramics with printed metals such as Ag, Au or Cu at $T \leq 1000°C$.[60, 61]

As shown in Fig. 24, the LTCC fabrication process initiates with flexible ceramic tapes in a green state, which are cut to the required size (typically 100-200 mm square). Vias and cavities are then punched in the blank tiles and filled with a paste of metals, such as Ag, Au or Cu.[60, 61] Subsequently, the required pattern is printed with a conductive paste. Once all of the layers have been produced individually, the layers are collated in to a stack, laminated under pressure, sintered, and cut to individual pieces.

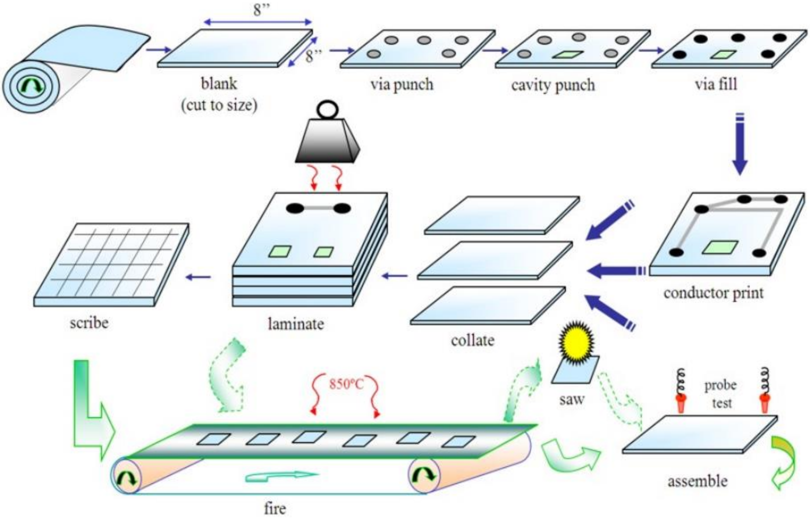

Figure 24. Process flow of a LTCC substrate.[60]

The substrates employed in microelectronic packages must fulfill the following requirements:[60]

a) Low dielectric constant to minimize crosstalk and signal delays;[62]

b) The coefficient of thermal expansion must match with the silicon semiconductor ($3.5x10^{-6}/^{o}C$) maintaining the reliability of the connection of the interconnects (board and components);

c) Ability to withstand the manufacturing temperature (500-1000 °C);

d) High mechanical strength to withstand the stresses during manufacture, as well as while in use;

e) Physical and chemical compatibility between the conductor and substrate to have good adherence during the firing [63]

The advantages of the LTCC process are the flexibility in design, the possibility to tailor dielectric properties through composition; LTCC can be suited to high volume production, and low cost due to the possibility of parallel manufacturing and low firing temperature. [61, 64]There are also some limitations for LTCC technology: As the substrates are not polished, the surface roughness can result in transmission loss, i.e., the conduction path of the conductor becomes longer. A high control of the process must be taken to avoid substrate warping during fabrication and the presence of carbon residues must be prevented as carbon reduces insulating properties. [61, 65]

Commercial substrates fabricated using LTCC technology are shown in Table 5.[61]

Table 5. Glass-ceramic substrates from different companies fabricated using LTCC technology.

LTCC Suppliers	**Products (composition)**	**Dielectric constant (c)**	Resistivity (Ω*cm)	**Thermal expansion coefficient (ppm/ °C)**	**Thermal conductivity (w/m*K)**	**Flexural strength (MPa)**	**Firing Temperature (°C)**
Asahi glass	$35Al_2O_3$ $+ 25$Forserite $+ 40$NSG (wt.%)	7.4	$>10^{14}$	5.9	4.2	235	900-1000
Kyocera	$BSG + SiO_2$ $+ Al_2O_3$ + Cordierite	5.0	$> 10^{14}$	4.0	2	190	
	Crystallized glass $+ Al_2O_3$	6.2	$> 10^{14}$	4.2	3	210	
Dupont	$Al_2O_3 + CaZrO_3$ + Glass	8.0	$> 10^{12}$	7.9	4.5	200	

CFG are composites of glass matrix reinforced with ceramics. Borosilicate glasses show a higher voltage isolation compared to alumina[1, 2] (ε=4 and ε=9 at 1MHz, respectively), a higher electrical stability under an electric field, CTE of $3.5.10^{-6}.^{o}C^{-1}$ reducing the differential thermal expansion strain at the semiconductor (Si)-insulator (CFG) interface, and a sintering temperature of around 800°C. When alumina is used as filler in CFG [2, 8], the combination of borosilicate glass and alumina results in a material with a higher thermal stability and mechanical resistance in comparison to pure glass.[11]

Due to the chemical and physical properties and the low sintering temperature, CFG composites could represent low-cost alternative to ceramics to be used as substrates using the LTCC technology.[10]

2.10 Characterization methods studied

2.10.1 Flexural strength

Flexural strength is a mechanical parameter for brittle materials. It is defined as a material's ability to resist deformation under load. Fracture of polycrystalline ceramics at room temperature is occurring by initiation from inherent flaws and fracture stress. Flexural strength, σ, is governed by the Griffith-Orowan relationship. [66]

$$\sigma = \frac{E\gamma}{\sqrt{\pi c}} \tag{12}$$

where:

E= Young´s Modulus
γ=Fracture energy
c= Flaw size

For composites, the value of E can be estimated using the rule of mixtures while fracture energy can be estimated from the fracture toughness, K_{Ic}, and Young´s Modulus using the relationship:

$$\gamma = \frac{K^{2}}{2E} \tag{13}$$

Flexural strength can be determinate by three- or four-point transverse bending test. Fig. 25 shows a schematic representation of a three-points transverse bending test equipment used to determine flexural strength.

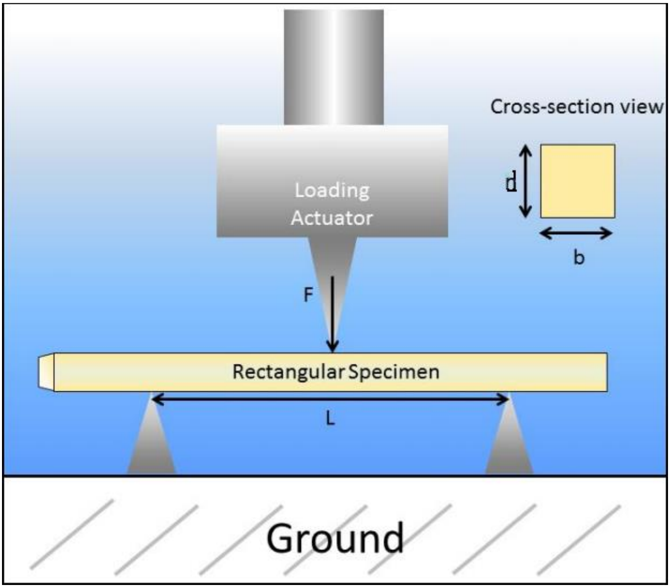

Figure 25. Schematic representation of a three-points transverse bending test equipment.[49]

The flexural strength represents the highest stress experienced within the material at its moment of rupture. A uniaxial load is applied on a bar specimen and recorded as function of the strain. The specimen is placed on two supports that are a distance apart (L), and the actuator applies a load in the middle of the two supports (L/2). Width and height of the specimen are b and d, respectively. Immediately before failure, the equipment records a force (F_f), and a deformation in mm. The flexural strength (σ) of the specimen is calculated using the following equation [67]:

$$\sigma_{rf} = \frac{3F_f L}{2bd^2} \tag{14}$$

2.10.1.1 Weibull Modulus

The Weibull distribution is a probability analysis and is one of the most widely used lifetime distributions in reliability engineering. Weibull developed a statistical model based on the following expression:[67, 68]

$$F = 1 - exp\left[-\left(\frac{\sigma}{\sigma_0}\right)^m\right] \tag{15}$$

where F is the probability of failure, σ_0 the strain at which 63.2% of samples tested brake in and *m* is the Weibull module, which is a constant related to measurement repeatability. F can be calculated by the expression:

$$F = \frac{n}{N+1} \tag{16}$$

where N is the number of samples used and *n* is the ranking of the sample ranging from 1 to N. To determine the parameters of Weibull (σ e *m*), ln[ln(1/(1-F))] is plotted as function of flexural strength(σ) using the equation 17.[67]

$$ln\left[ln\left(\frac{1}{1-F}\right)\right] = mln\sigma - mln\sigma_0 \tag{17}$$

In the plot *m* is the slope of de curve. The greater the *m* value, the lower the dispersion of flexural strength values. Measurements made with higher Weibull modulus will exhibit higher reliability and their strengths are distributed uniformly throughout the material.

2.10.2 Fracture toughness

Fracture toughness describes the ability of a material containing a crack to resist fracture. Metals energy dissipation at the crack tip occurs via plastic deformation through dislocation. Brittle materials such as ceramics and glasses not deform plastically, and absorb relatively little energy prior fracture during crack propagation.[69]

The fracture toughness can be determined using a Vickers indentation fracture formulation based on an ideal "sharp indenter" geometry (see Fig. 26).

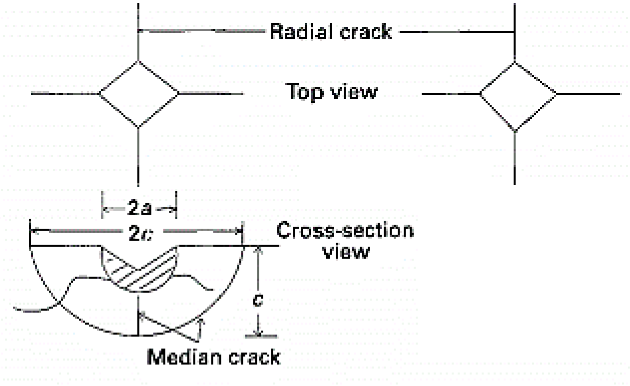

Figure 26. Top and cross-section views around Vickers indent as median cracks.[66]

The indentation measurement model can be used for the determination of fracture toughness (K_{Ic}) in glasses and ceramics, and the obtained results are comparable to those obtained using the notched beam technique (NBT)[67]. Fracture toughness can be calculated using Lawn and Fuller´s model, which has the following equation[67, 71]

$$K_{IC} = \frac{P/c^{3/2}}{\pi^{3/2}\tan\psi} \tag{18}$$

where P is the contact load, c is the crack length as shown in Fig. 26, ψ is the half-angle of the indenter between opposing pyramid edges equal to 68^o .

2.10.3 Dielectric constant

A material exhibits capacitance (C) or “dielectricity” if it has the ability to store energy when an external electric field is applied. If a DC voltage source V is applied across a parallel plate capacitor (Fig.27), more charge is stored when a dielectric material is placed between the plates with respect to vacuum (no material between plates).

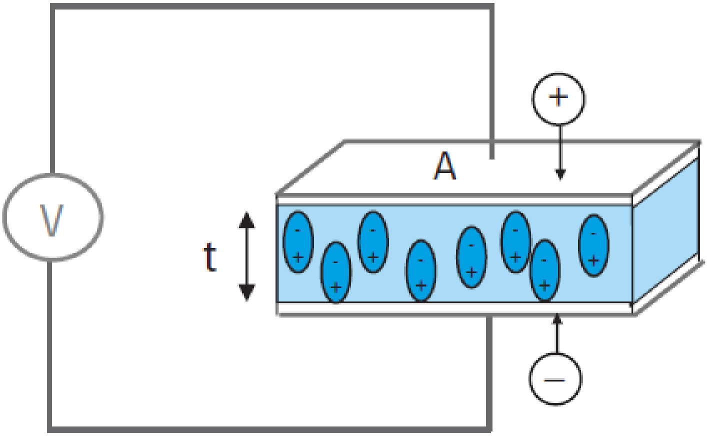

Figure 27. Schematic representation of a parallel plate capacitor.[72]

Permittivity is the measure of the resistance that is encountered when forming an electric field in a medium. The permittivity of a medium describes how much electric field (more correctly, flux) is 'generated' per unit charge in that medium. Permittivity depends on frequency of the field applied, temperature, molecules orientation, atmospheric pressure, and molecular structure of the material.[67]

Coulomb’s law is physics’ law which describes the electrostatic interaction between electrically charged particles. The law states if there is an electric field due to a single point A of charge of value q [C] at a distance $R(m)$ (see Fig. 28), the effect of the electric-field is directly proportional to the product of the magnitudes of the charge and inversely proportional to the square of the distance between the charge and the point, with a Coloumb force constant of proportionality k, $k = 1/(4\pi\varepsilon_0)$.

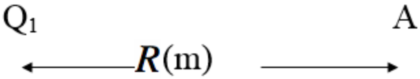

Figure 28. Scheme of a electric field of a single point A of charge of value *Q* [C] at a distance *R(m):*

$$|E| = k\frac{q}{R^2} = \frac{q}{4\pi\varepsilon_r\varepsilon_0 R^2} = \frac{q}{4\pi\varepsilon R^2} \qquad (19)$$

where ε_0 is the permittivity of free space(vacuum), which is a constant measured in Farads/meter. ε_r is known as the dielectric constant or relative permittivity.

The permittivity of a medium is expressed as the product of the dielectric constant and the free space permittivity:[67]

$$\varepsilon = \varepsilon_r\varepsilon_0 \qquad (20)$$

The dielectric constant is always greater than or equal to 1. That means the electric field in equation 19 is always reduced relative to the electric field in free space.[67]

The method that can be used to measure the dielectric constant is the parallel plate method. A thin sample of a solid material or liquid placed between two electrodes to form a capacitor can be used to determinate the dielectric constant. Capacitance is measured automatically, then is used to calculate dielectric constant using equation 21.

$$C = (\varepsilon_0\varepsilon_r \mathrm{A})/\mathrm{D} \qquad (21)$$

where ε_r is the dielectric constant of the material, ε_0 is $8{,}854 \times 10^{-12}$ F.m^{-1}, A is the specimen area and D the thickness of the specimen, that is, the distance between plates.

3. MATERIALS AND EXPERIMENTAL PROCEDURES

3.1 Materials

Alumina-filled borosilicate glass composites were produced using powders of borosilicate glass as matrix and aluminum oxide, alumina (Al_2O_3) as filler.

3.1.1 Borosilicate glass

Chemical composition, weight percent (wt.%) and some physical data of commercial borosilicate glass ($79SiO_2$, $13B_2O_3$, $4Na_2O$, $2.5Al_2O_3$) (Pyrex®) used in this work are shown in Table 6 and Table 7, respectively.

Table 6. Typical chemical composition of borosilicate glass. [73]

Chemical composition (wt.%)	
SiO_2	79.84
B_2O_3	12.76
Na_2O	4.19
Al_2O_3	2.50
CaO	0.09
Fe_2O_3	0.06
BaO	< 0.1
K_2O	0.10
Co_2O_3< 0.1	
MgO	< 0.05
Cr_2O_3< 0.1	
MnO	< 0.05
PbO	< 0.1
SrO	0.07
P_2O_5< 0.05	
ZnO	< 0.1

Table 7. Physical data of commercial borosilicate glass (Pyrex®).[73]

Coefficient of mean linear thermal expansion α (20 -300 °C)	3.3 x 10^{-6} K^{-1}
Dielectric constant (at 1 MHz)	4.1
Glass transition temperature T_g	525 °C
Softening point (at viscosity η in Pa x s:$10^{7.6}$)	825 °C
Density	2.23 g.cm^{-3}

Borosilicate glass powder was obtained by dry ball milling of glass cullet during 1 to 3 h at 80 rpm using an alumina jar of 10 cm diameter and Al_2O_3 balls (ϕ= 10-30 mm). The ball to powder weight ratio was 1:3. After milling, powders were sieved with water with 230, 550 and 625 mesh sieves, and dried for 48 h at 90°C. The presence of cristobalite can be detected by XRD (see Fig. 29).

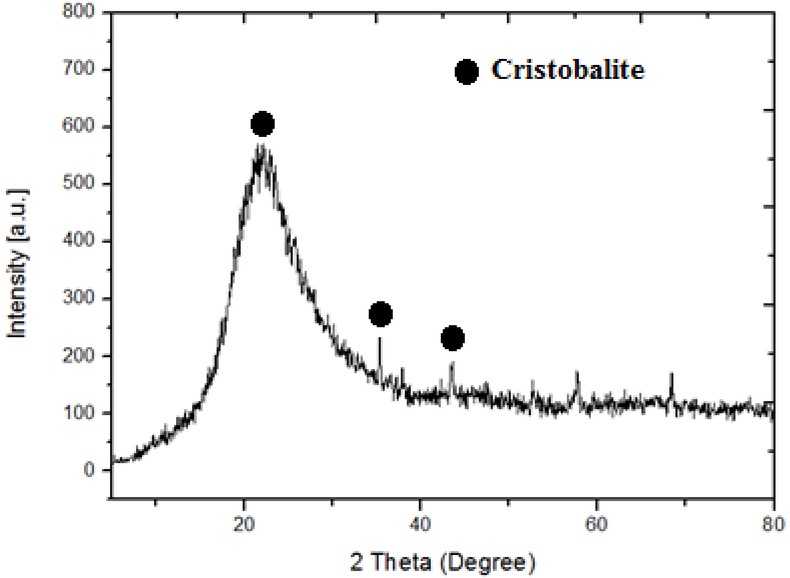

Figure 29. XRD analysis of ball-milled borosilicate glass.

3.1.2 Aluminum oxide

The material used as filler was high purity (>99.7 wt.%) alumina powder (Almatis Alumina Premium, Netherlands), with particle size varying from 0.3 to 3 μm. Table 8 and 9 show its chemical composition as informed by the manufacturer and the main physical properties of alumina, respectively.

Table 8.Chemical composition of as received alumina (wt.%)

Al_2O_3	99.7
Na_2O	0.06
Fe_2O_3	0.02
SiO_2	0.01
CaO	0.01
B_2O_3	0.01

Table 9. Physical properties of as received alumina

Coefficient of mean linear thermal expansion α (20 - 300°C)	$8.9x10^{-6}$ K^{-1}
Dielectric constant (at 1 MHz)	9.1
Melting point	2070 °C
Density	3.94 $g.cm^{-3}$

3.2 Powder characterization

3.2.1 Particle size and particle form

The particle size distribution of borosilicate glass after milling and as received alumina powder was determined using a Malvern Mastersizer 2000 and a Malvern Zetasizer ZS90 equipment. Suspensions containing 1 vol.% of powder, 98.5 vol.% distilled water, and 0.5 vol.%

of Dolapix CE 64 (Zschimmer & Schwarz, Lahnstein/Rhein, Germany) used as dispersing agent, were analyzed. The particles morphology was characterized by Scanning Electron Microscopy (SEM, Hitachi TM3030).

3.2.2 Powder density (true density)

The density of glass powder after milling was determined using a helium picnometry (a1305 Micromeritics). The density measurement was performed 10 times.

3.3 Samples preparation

3.3.1 Uniaxial pressing

Powder mixtures containing borosilicate glass and 0, 5, 10, 15, 20 vol.% alumina, and 3 wt.% isopropyl alcohol were mixed for 1 h at 100 rpm using a PVC jar and silicone balls (ϕ= 10 mm). The ball to powder weight ratio used was 1:3. After mixing, powders were sieved, uniaxially pressed in a steel die at 15 MPa, and dried at 60 ^{o}C during 24 h, resulting in bars of 40 x 5 x 4 mm. The green density was determined geometrically on three samples and the arithmetic mean value with the standard deviation was calculated.

3.3.2 Sintering

The green samples were conventionally sintered in air using an electric furnace at 800 to 1000^{o}C, and holding times varying from 0 to 10 min, heating rates of 1 to 15^{o}C/min and cooling rate of 10^{o}C/min. Samples were also sintered using the *Fast Firing* procedure introducing green samples in the pre-heated furnace at 850 to 1000^{o}C, using holding times of 3 to 7 min with heating rate of approximately 500^{o}C/min, 3 samples were used for each parameter change.

3.3.3 Tape casting

Slurries of powder mixtures containing 5 and 10 vol.% alumina were produced following the experimental procedure as presented in reference [3] First 50 wt.% solids were mixed with 27 wt.% distilled water, 1 wt.% deflocculant (Darvan 821A, EUA), and 0.05 wt.% anti-foam (Sigma-Aldrich-Germany) was added. The slurry was milled for 4 h at 100 rpm using a PVC jar and silicone balls (ϕ= 10 mm). The ball to liquid weight ratio was 1:3. Then 21.95 wt.% binder (Mowilith® containing 20 wt.% dibutyl phthalate plasticizer) was added and mixed for 30 min.

Tapes were produced using a tape casting machine (Richard E. Mistler, Inc., CC-1200, EUA), by casting the slurry on polyethylene terephthalate (PET) Mylar carrier film coating with a fine silicone layer (G10JRM, Mistler). The casting speed was 6 cm/min and the gap between the blade (doctor blade) and the carrier was adjusted manually to obtain a tape thickness of 900 µm. The tapes, after drying, was then dried at room temperature for 24 h, and detached from the film.

The rheological behavior of the slurries was measured in a rotational viscometer (System/52p, Rheomex, Haake) with concentric cylinders geometry and at room temperature. The rheograms of the slurries were made with a shear rate of 0.02 to 50 s^{-1}. The apparent viscosity was determined by best fit to the curves of Casson´s model [74].

3.3.3.1 Tape debinding and sintering

Debinding of the green tapes was obtained heating at 1°C/min up to 500°C using a holding time of 30min. Afterwards the tapes were heated to sinter from 500°C to 800°C holding time of 5 min using a heating rate of 15°C/min.

3.4 Sample characterization

3.4.1 Thermal treatments

Dimensional changes of the borosilicate glass powder as function of temperature and time was analyzed using dilatometry analysis (DIL, Netzsch DIL 402 C, Germany). Differential scanning calorimetry analyses (DSC, Netzsch DSC 404 F1, Germany) was also performed. The sintering temperature, glass transition temperature, softening point, crystallization and phase changes temperatures were determined at temperatures ranging from 30 to 1000°C using heating rates of 2 and 15 °C/min.

3.4.2 Bulk density

The bulk density of sintered samples was measured in water using the Archimedes´ Principle. The density was determined on 3samples, 3 times each, and the arithmetic mean value with the standard deviation was calculated.

3.4.3 Determination of flexural strength

The flexural strength of sintered samples was determinate at room temperature by using a loading speed of 1 mm/min, using only 10 samples for each determination, due to the difficulty in assembling green samples and their fragility while managing. The flexural strength (σ) was calculated using the following equation:

$$\sigma_{rf} = \frac{3F_fL}{2bd^2} \qquad (22)$$

where F_f is the maximum load, L the distance between the supports, 42 mm in this case, and b and d are width and high of the sample, respectively.

The Weibull module was determined as explained in Section 2.10.1.1.

3.4.4 Determination of fracture toughness

The fracture toughness was measured at room temperature using the indentation method as described in Section 2.11.2, in 3 samples processed at the same conditions. Three different places of the same sample were indented, and the arithmetic mean value with the respective error was calculated.

A standard microhardness tester with a Vickers diamond pyramid and indenter loads of 10 N were used. With the diamond indenter in position nearly touching the sample, the indenter was released using a loading rate of 2 mm/min. After 5s the indenter was removed. Using the graticule scale of an optical microscope (Shimadzu) the length of the cracks extending from the pyramidal diamond indenter impression corners was measured. Using the Lawn and Fuller´s model described in the section 2.11.2, the fracture toughness (K_{Ic}) was determined.

3.4.5 Determination of Vickers Hardness (HV)

The Vickers hardness of sintered samples were determined using a Vickers Hardness tester (HMV-Shimadzu, Microhardness Tester) on samples using a load of 5 N, in 3 samples processed at the same conditions. Three different places of the same sample were indented, and the arithmetic mean value with the standard deviation was calculated

The HV number was determined by the ratio F/A, where F is the force applied to the diamond in kilograms-force and A is the surface area of the resulting indentation in square millimeters.

3.4.6 Determination of the coefficient of thermal expansion

The coefficient of thermal expansion from 25 to 300^{o}C of borosilicate glass and CFG composites was determined in sintered samples heated at 7.5^{o}C/min using a Pushrod Dilatometer (Netzsch, Mod. DIL 402 C).

3.4.7 Determination of the dielectric constant

Dielectric constant of 3 sintered samples at the same conditions were determined by parallel plate method, using an LCR meter Agilent E4980A equipment (Keysight technologies). Cylindrical samples of diameter ϕ=20 mm and height h=1.5 mm, were placed between two electrodes of ϕ=20 mm. The capacitance (Cp) was measured at a frequency of 1 MHz and amplitude of 1V. The dielectric constant was calculated with the equations presented in Section 2.10.3.

3.4.8 X-ray diffraction

X-ray diffraction at room temperature was performed in powdered samples and diffraction angles 2θ between 10° and 105°, using a Rigaku Desktop Miniflex II (30KV, 15mA, Cu Kα radiation).

3.4.9 Scanning electron microscopy

Polished samples were etched in a solution with hydrofluoric acid 2 wt.% for 2 min and coated with gold. Analyses were performed using SEM, Hitachi TM3030.

4. Security

The lab commitment to safety and environmental protection is priority. Therefore, to maintain the environmental safety and security of the lab and its researchers, some procedures were implemented:

a) Before using a reagent, its security datasheet was analyzed and followed according to its hazardous degree. When necessarily, appropriated equipment was used. For example, Fig. 30 shows the exposure controls section of hydrofluoric acid datasheet used for etching polished samples for SEM observations. In this case was needed the use of exhaust ventilation, impervious gloves, chemical resistant goggle, lab coat and boots.

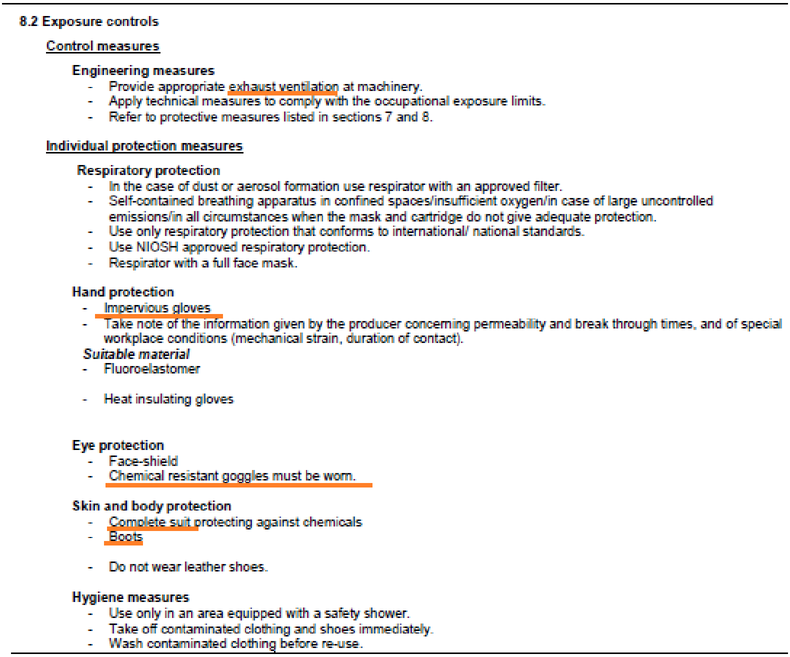

8.2 Exposure controls

Control measures

Engineering measures

- Provide appropriate exhaust ventilation at machinery.
- Apply technical measures to comply with the occupational exposure limits.
- Refer to protective measures listed in sections 7 and 8.

Individual protection measures

Respiratory protection

- In the case of dust or aerosol formation use respirator with an approved filter.
- Self-contained breathing apparatus in confined spaces/insufficient oxygen/in case of large uncontrolled emissions/in all circumstances when the mask and cartridge do not give adequate protection.
- Use only respiratory protection that conforms to international/ national standards.
- Use NIOSH approved respiratory protection.
- Respirator with a full face mask.

Hand protection

- Impervious gloves
- Take note of the information given by the producer concerning permeability and break through times, and of special workplace conditions (mechanical strain, duration of contact).

Suitable material

- Fluoroelastomer

- Heat insulating gloves

Eye protection

- Face-shield
- Chemical resistant goggles must be worn.

Skin and body protection

- Complete suit protecting against chemicals
- Boots

- Do not wear leather shoes.

Hygiene measures

- Use only in an area equipped with a safety shower.
- Take off contaminated clothing and shoes immediately.
- Wash contaminated clothing before re-use.

Figure 30. Exposure controls section of hydrofluoric acid datasheet, and the protection apparatus used as underlines.

b) When fast firing experiments had been scheduled, people working in lab facilities were previously warned to keep away from the furnace room. The security material used by the operator consisted in a high thermal resistant suit, face-shield, boots, gloves and long tweezers to maintain distance from the heat furnace. See Fig. 31.

Figure 31. Fast firing procedure.

In each experiment, the appropriated measurements as response and neutralizers were in place in case of accident.

5. RESULTS AND DISCUSSION

5.1 Powder characterization

5.1.1 Borosilicate glass

The effect of milling time on particle size of borosilicate glass was analyzed. As shown in Fig. 32 the particle size (D_{50}) varies with milling time (t) according to equation indicated in the graph.

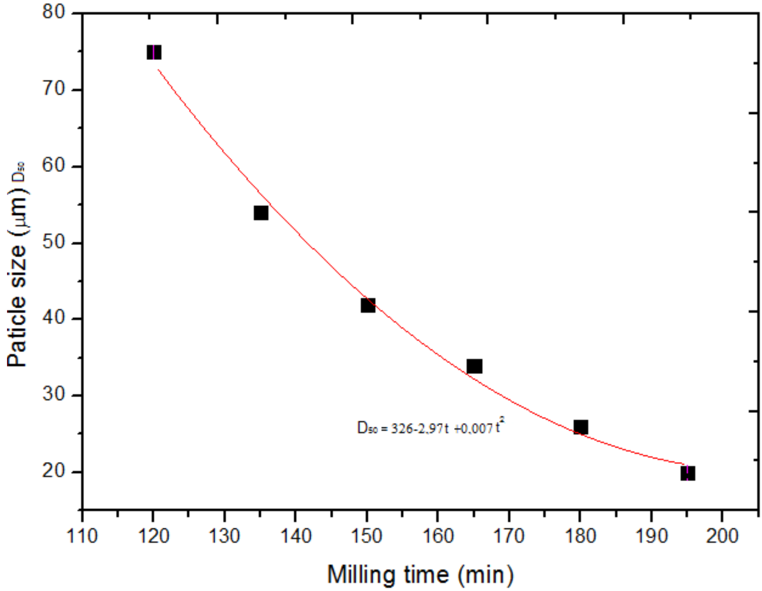

Figure 32. Particle size of borosilicate glass as function of milling time.

Fig. 33 shows particle size distribution of borosilicate glass after milled for 195 min.

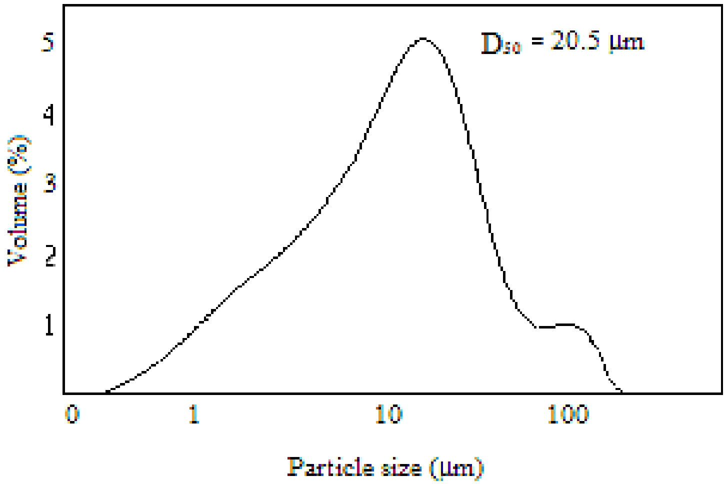

Figure 33. Particle size distribution of borosilicate glass after milled for 195 min.

The curve shows a bimodal distribution, with most of the particles showing sizes up to 20 µm.

The morphology of borosilicate glass particles after milling was characterized by scanning electron microscopy (SEM). As presented in Fig. 34 particles show an irregular form.

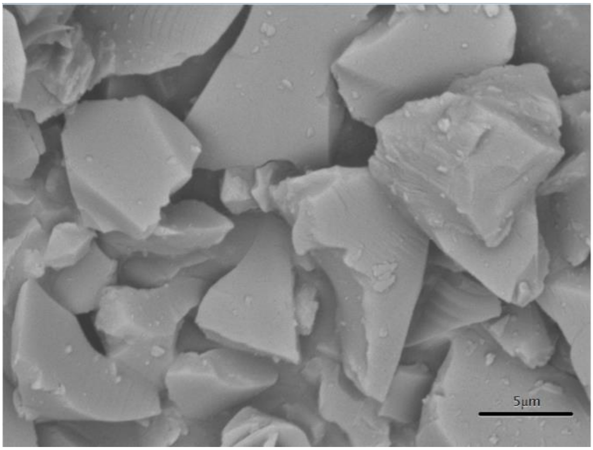

Figure 34. SEM image of borosilicate glass particles after milling for 195 min.

5.1.2 Alumina

Fig. 35 shows the particle size distribution of alumina as received.

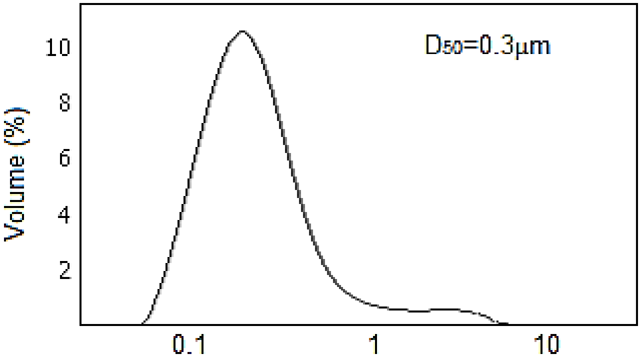

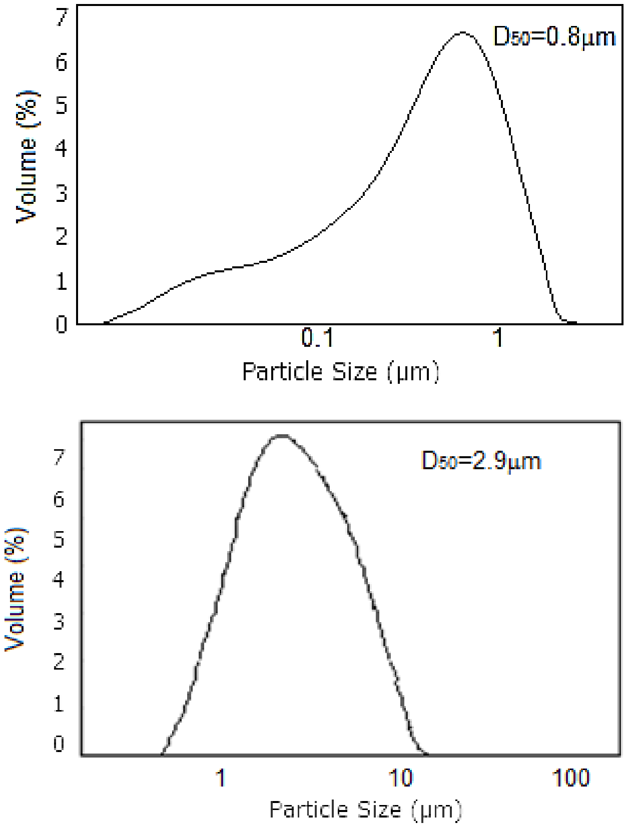

Figure 35. Particle size distributions of as received Almatis Premium Alumina.

The curve shows a narrow distribution of alumina particles and sizes of D_{50}=0.3, 0.8 and 2.9 µm. As presented in Fig. 36 aluminum oxide particles have a platelet-like form.

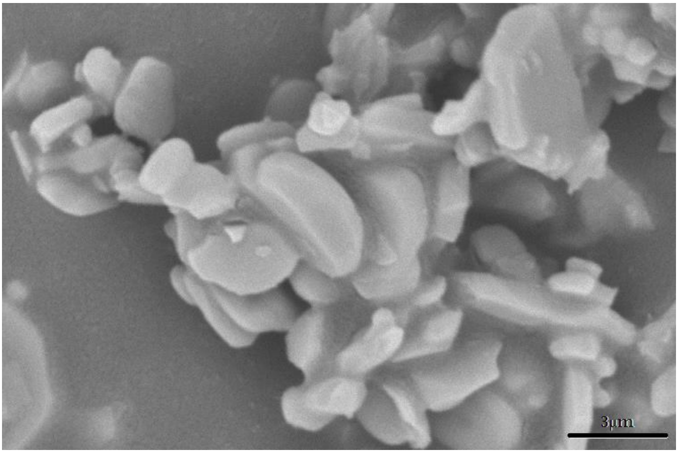

Figure 36. SEM image of as received aluminum oxide powder.

5.1.3 Powder density and green density of samples after pressing

Powder density as determined using helium was 2.223 ± 0.003 g/cm³ for borosilicate glass and 3.966 ± 0.005 g/cm³ for alumina. The geometrical density (green density) of samples after pressing is shown in Table 10.

Table 10. Green density of pressed samples

Material	Green density(g/cm^3)	Density, th.(%)
Borosilicate glass	1.16 ± 0.16	52
Borosilicate glass + 5 vol.% alumina	1.32 ± 0.21	55
Borosilicate glass + 10 vol.% alumina	1.34 ± 0.34	56
Borosilicate glass + 15 vol.% alumina	1.29 ± 0.31	52
Borosilicate glass + 20 vol.% alumina	1.36 ± 0.23	53

5.2 Conventional sintering

5.2.1 Dilatometric and DSC analysis

Dimensional changes during heating and sintering of borosilicate glass compacts fabricated using powder of particle size of 20 µm was analyzed using dilatometry. Fig. 37 shows the dimensional change of a compact heated at 15°C/min.

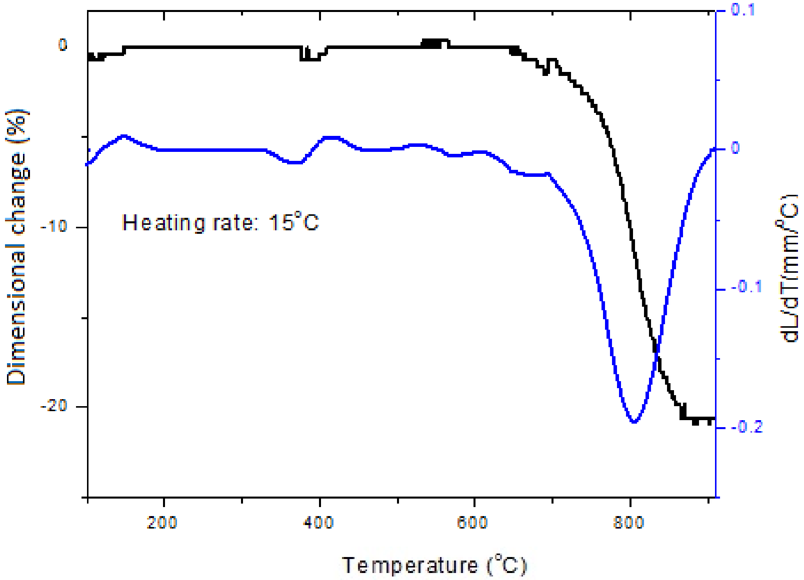

Figure 37. Dilatometric analyses of a borosilicate glass compact heated at indicated heating rate.

Fig. 37 shows that the compact begins to shrink at ~670 °C, the softening point of borosilicate glass [1] the sample reach the maximum velocity of shrinkage at ~810 °C, and that sintering finishes at ~900 °C, where ΔL/ΔT=0. The temperature region where the maximum velocity of shrinkage was observed, namely 800 and 850 °C, have been chosen for further sintering studies.

Fig. 38 shows the DSC analysis of the borosilicate glass heated at 2 °C/min.

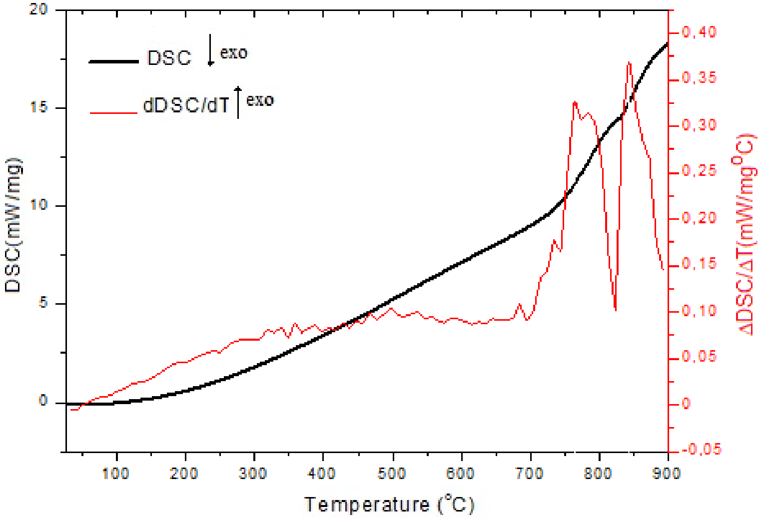

Figure 38. DSC analysis of borosilicate glass heated at 2 °C/min.

In the dDSC/dT curve in Fig. 38 two exothermic peaks are observed at ~700 to ~820 °C and ~820 to ~900 °C, related to crystallization at those temperatures ranges.[75]

5.2.2 Sintering

The effect of the particle size of borosilicate glass on densification was analyzed. Fig. 39 shows the relative density of borosilicate glass compacts after sintering at 800°C.

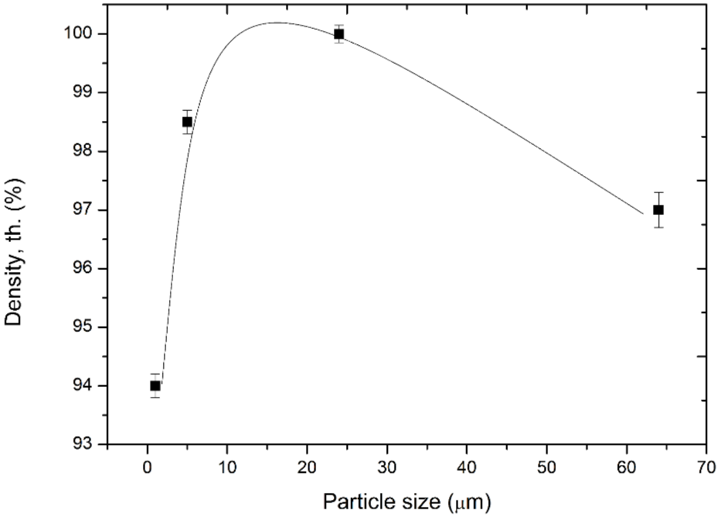

Figure 39. Relative density of borosilicate glass samples after sintering at 800 °C as function of particle size.

Fig. 39 shows an increase in densification up to 20 μm, and above a decrease in glass sintering related to the larger particle size, which demands a higher energy to sinter when compared to the other sizes. Fig. 40 shows XRD of borosilicate glass sintered samples revealing a higher peak with particle size of 1 μm. Fig. 41 shows a SEM image of the microstructure after sintering of the samples, varying borosilicate particle size of 1, 20 and 64 μm.

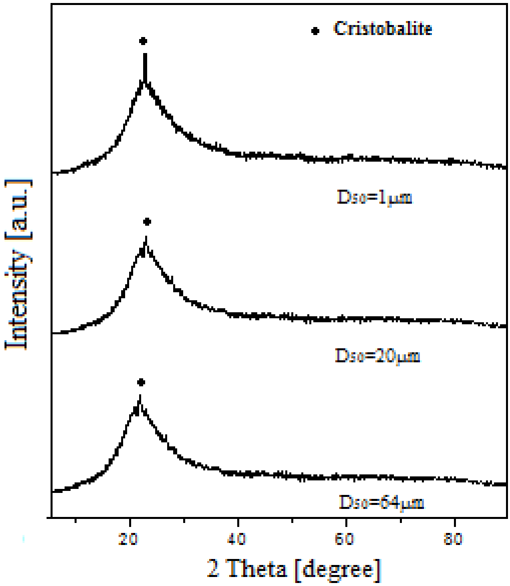

Figure 40. XRD of sintered borosilicate glass at indicated particle sizes.

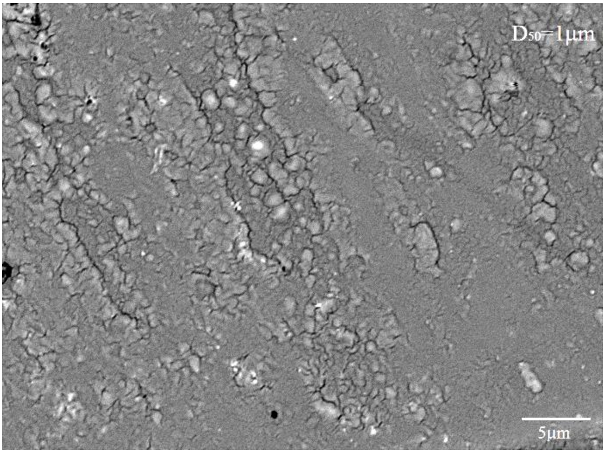

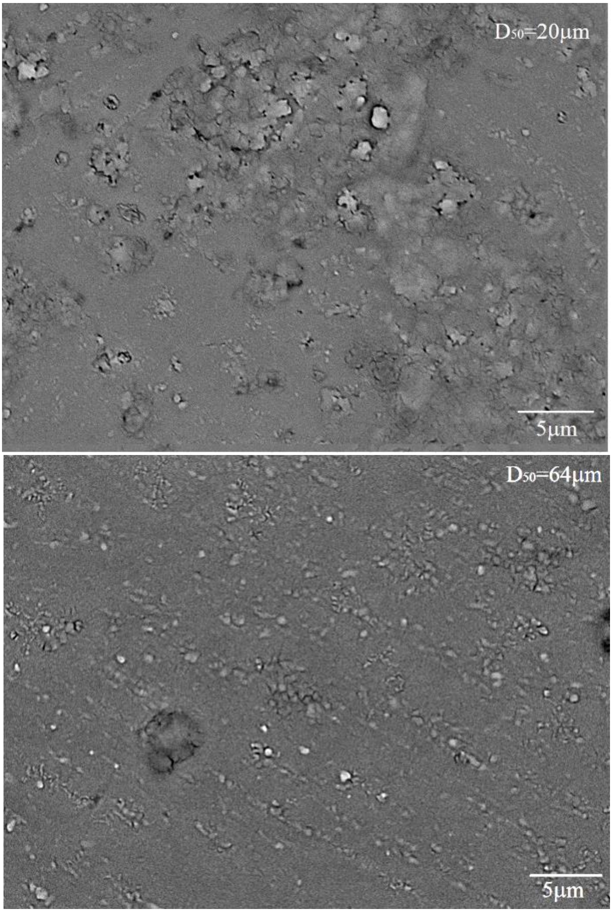

Figure 41. SEM image of borosilicate samples fabricated using powders of particle size as indicated, heated at 10 °C/min to 800 °C and sintered for 5 min.

Fig. 41 shows a microstructure with more cristobalite formation for samples sintered with glass particle size of 1 μm. The image with glass particle size of 64 μm shows cristobalite formation though with a smaller size when compared to the first image, another reason for decreasing the glass sintering is the bigger particle size, which demands a higher energy to sinter than other. Fig. 40 and 41 show the effect of borosilicate particle size on sintering, as cristobalite is formed, presenting a slight decrease in crystallization with increasing particle size above size of 20 μm.

The effect of heating rate on the densification of borosilicate glass powder of particle size of 20 µm was investigated using heating rates of 1 to 15°C/min, and is shown in Fig.42.

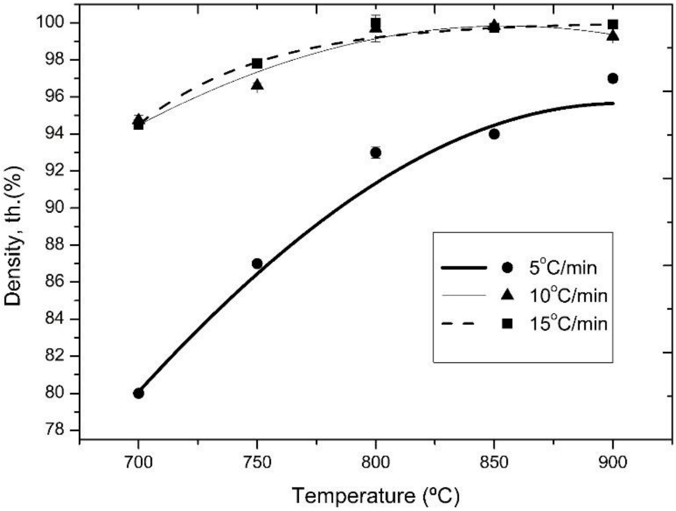

Figure 42. Relative density of borosilicate glass samples sintered for 5 min at indicated temperatures using heating rates of 5, 10 and 15 °C/min.

In Fig. 42 an increase in densification with increasing heating rate is observed. The determination of density on samples sintered using heating rates of 1 and 3°C/min was not possible due to the high brittleness of the samples. The observed decrease of sinterability with decreasing heating rate is related to the crystallization of cristobalite, as presented in Fig.43.

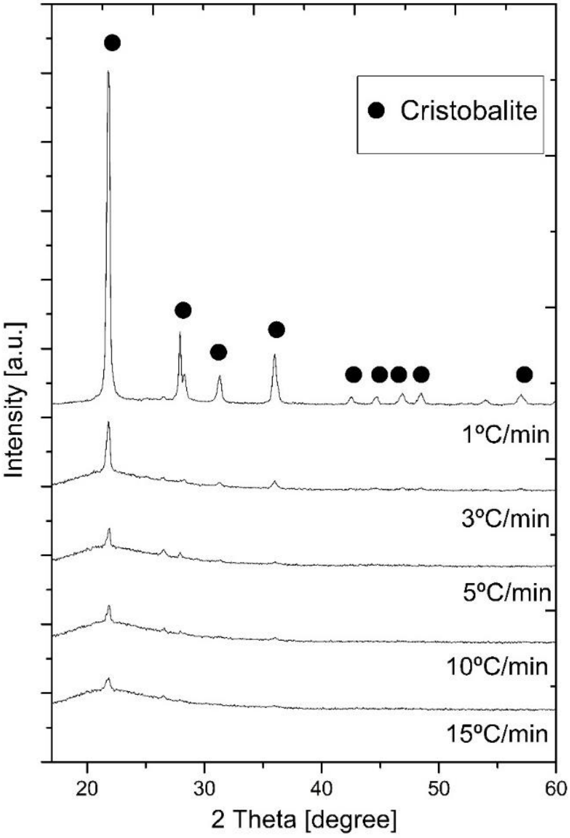

Figure 43. XRD of borosilicate glass, sintered at 800°C, using a holding time of 5 min and the indicated heating rates.

As shown in Fig. 43, the amount of cristobalite formed is inversely proportional to the heating rate. This behavior can be explained by the time in which samples have to diffuse for nucleation and crystallization until reaches maximum temperature. The formation of cristobalite affects densification. If crystallization occurs before full densification, the reduction of viscous flow of the system hinders densification and a porous body is obtained [75].

Fig. 44 shows SEM images of the microstructure of the samples after sintering, using heating rates from 5 to 15 °C/min.

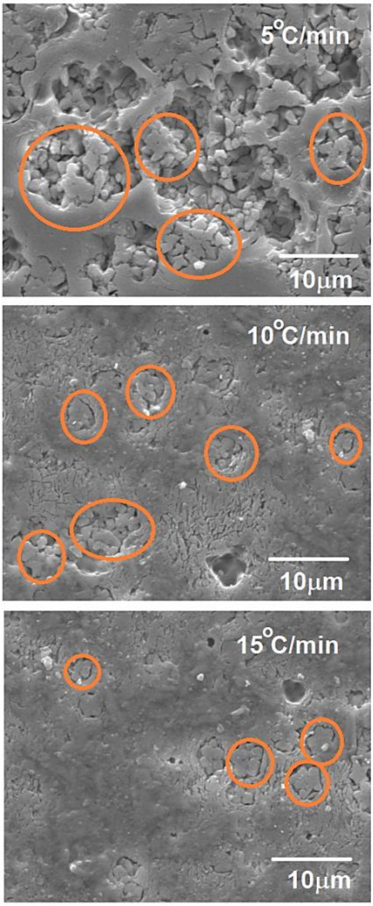

Figure 44. SEM images of borosilicate glass, sintered at 800 °C, holding time of 5 min, varying the heating rate as indicated. Red circles show cristobalite crystals.

Fig. 44 shows the characteristic “flower” form of cristobalite. The increase in heating rate hinders crystallization, both the size and quantity of cristobalite decreases with increasing heating rate.

The effect of holding time and sintering temperature on densification was analyzed.

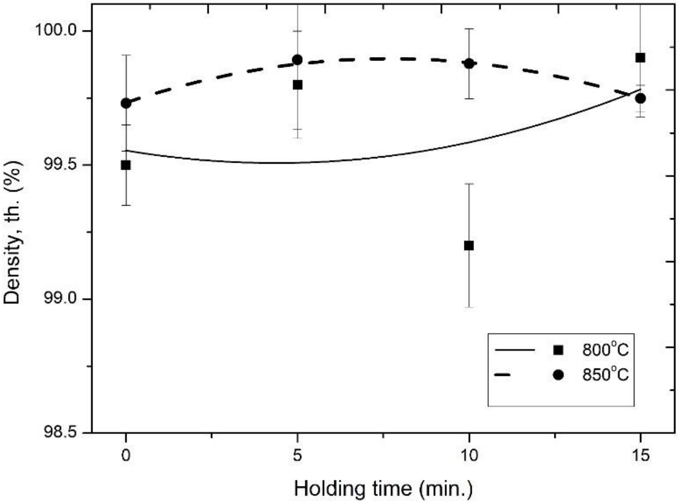

Figure 45. Relative density as function of sintering time for borosilicate glass powder compacts, heated at 15°C.min^{-1} up to indicated temperature.

As shown in Fig. 45 the highest density obtained was 99.6 th.% ± 0.4 after sintering for 5 min at 800°C.

5.2.3 Conventional sintering of borosilicate glass and alumina compacts

The effect of the content and particle size of alumina on the densification of borosilicate glass-alumina compacts was analyzed and results are shown in Fig. 46. Alumina powders with particles size (D_{50}) of 0.3, 0.8 and 3 μm were used, varying alumina content from 5 to 20 vol.%.

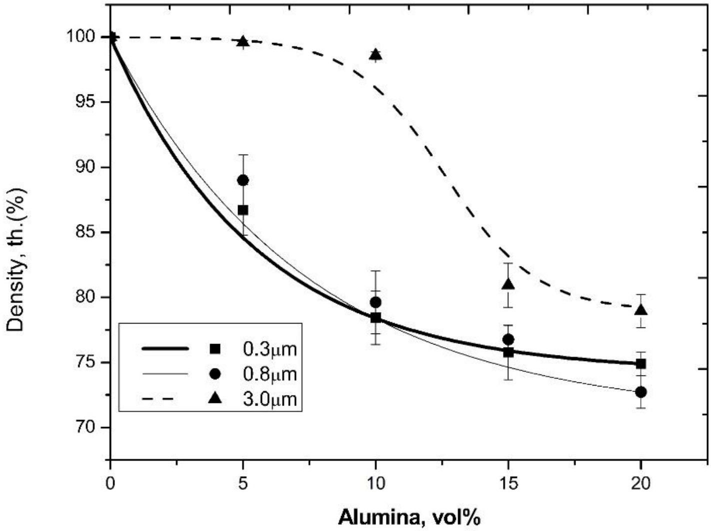

Figure 46. Relative density as function of alumina content of borosilicate glass compacts heated at 15 ºC.min^{-1} up to 800 ºC and held for 5 min, using alumina powders with particle size (D_{50}) as indicated.

The relative density of the composites decreases with the particle size and increasing amount of alumina. There are two possible motives for the behavior:

a) The presence of alumina acting as nondensifying inclusions giving rise to different sintering rates, and the development of transient and residual stresses that hinders densification. Causing porosity and leading to microstructural damage in the sintered material such as crack-like voids.[76]

b) The formation of a continuous network of inclusions reduces the sintering, inhibiting the densification. That phenomenon is related to the percolation threshold, i.e., the formation of long-range connectivity, which depends on the size ratio of the grain matrix and inclusion and inclusions content.[77] In a binary system such as proposed, using Bouvard and Lange´s model shown in Section 2.6, at a critical concentration of 2

> vol.%, inclusions start to contact with each other and form an extended rigid network. As the theoretical model considers the inclusions perfectly dispersed in the matrix, in our experiments some degree of alumina agglomeration could be present, contributing for the increases of the percolation threshold from 2 vol.% to 5 vol.%.

The effect of sintering temperature on the densification of borosilicate glass-alumina compacts (alumina, D_{50}= 3 μm) was investigated.

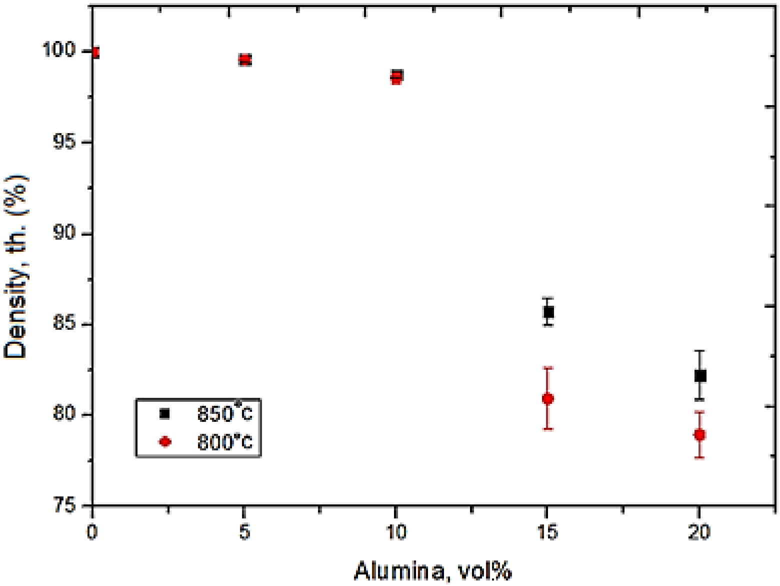

Figure 47. Relative density as function of alumina content in borosilicate glass powder compacts heated at 15 °C.min^{-1} up to indicated temperature and sintered during 5 min.

Samples containing 5 vol.% alumina show the highest density (99.0 ± 0.2 th.%). A decrease in the relative density above 5 vol.% alumina was observed.

The effect of alumina content on the crystallization of borosilicate glass during sintering of glass-alumina compacts was analyzed. Fig. 48 shows XRD of composites containing different amounts of alumina, sintered at 800°C during 5 min.

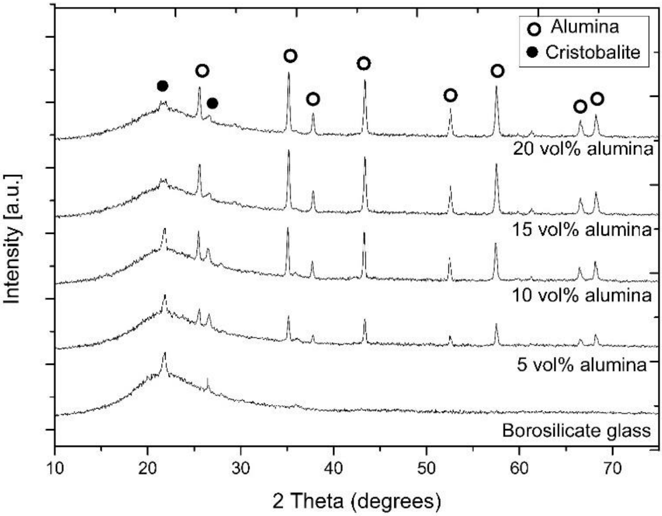

Figure 48. XRD of composites, sintered at 800°C, holding time of 5 min, varying alumina content as indicated.

Fig. 48 shows a decrease in the cristobalite with increasing of alumina content, indicating its influence upon crystallization. Na^+ cations are present in borosilicate glass composition (see Table 6), and its transport kinetics in Pyrex is known to be the rate-limiting step for devitrification.[5] Al^{+3}cations, present in alumina, are a network former, which can coordinate tetrahedrally with oxygen of SiO_4 presented in the glass structure. The negative charge created by the substitution of Si^{+4} by Al^{+3} in the glass network provides an electrochemical potential for alkali ions, maintaining electroneutrality at the local level, inhibiting Na^+ migration and cristobalite crystallization.

The microstructure of samples sintered at 800ºC during 5 min and heated at 15ºC/min was analyzed by SEM, and it is shown in Fig. 49.

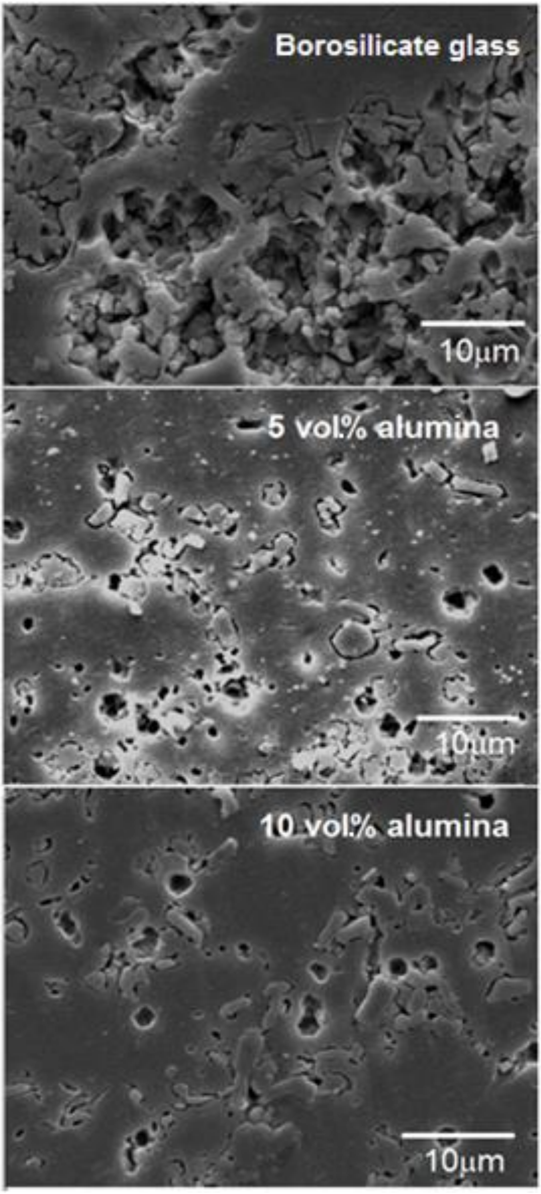

Figure 49. SEM images of borosilicate glass and composites samples conventionally sintered at 800ºC during 5 min and heated at 15ºC/min. Alumina content as indicated.

5.2.4 Coefficient of thermal expansion (CTE)

Using dilatometry analysis the CTE of sintered samples of borosilicate glass and CFG composites was determined between 25 and 300°C using a heating rate of 15°C/min. An increase in CTE was observed as the volume of alumina added increases. The CTE determined were 3.5, 4.9 and $5.4.10^{-6}$/°C for borosilicate glass, and composites containing 5 and 10 vol.% alumina, respectively. The increase in the CTE of CFG when compared to borosilicate glass, is related to the CTE of alumina which is 9.10^{-6}/°C, respectively.

Fig. 50 shows the theoretical CTE as function of cristobalite content, calculated using Turner´s model (in section 2.4). The experimental data are higher than theoretical data, due, probably, to the presence of cristobalite which has CTE of 10.10^{-6}/°C. In Fig. 50 is possible to observe the influence of cristobalite on the thermal expansion of the sintered materials. Considering only the presence of alumina and glass, the calculated CTE of CFG composites is 4.2 for 5 vol.% alumina and $5x10^{-6}$/°C for 10 vol.% alumina. The volume of cristobalite in the sintered samples can be estimated from Fig. 50 and from the experimental CTE data 3.5, 4.9 and $5.4x10^{-6}$/°C, for 0, 5 and 10 vol.% alumina, respectively. For glass, the estimation of cristobalite volume content is ~29%. For composites with 5 vol.% alumina content the cristobalite volume decreased to ~23%, and for 10 vol.% alumina, ~16%. Considering the content of cristobalite estimated from Fig. 50, after conventional sintering during 5 min at 800°C and a heating rate of 15°C/min, the actual relative density for borosilicate glass samples is 98%, and for composites containing 5 and 10 vol.% alumina 98% and 97%.

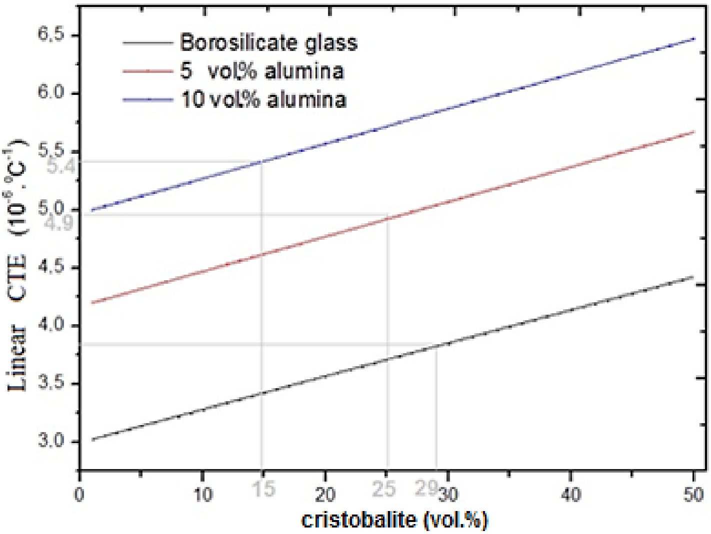

Figure 50. Theoretical linear CTE of borosilicate glass and CFG composites containing 5 and 10 vol.% alumina, as function of cristobalite content between 25 and 300°C.

5.2.5 Fast firing of borosilicate glass and alumina-filled borosilicate glass compacts

As shown previously in Fig. 42, using conventional firing increasing the heating rate increases densification and hinders crystallization. To investigate the effect on densification and cristobalite formation of the fastest heating rate possible to be used, compacts of borosilicate glass and borosilicate glass containing 5 to 20 vol.% alumina (D_{50}= 20 μm) were introduced in a pre-heated furnace at temperatures between 850° and 1000 °C and held during 3 to 7 min. Fig. 51 shows the relative density of borosilicate glass compacts after fast firing at indicated temperatures, as function of holding time and Fig. 52 shows the relative density of alumina-filled borosilicate glass composites after fast firing as function of alumina content.

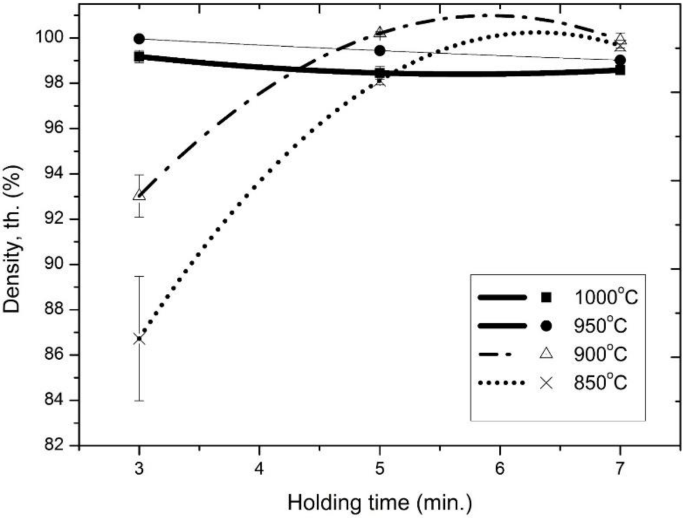

Figure 51. Relative density of borosilicate glass compacts as function of holding time after fast firing at indicated temperatures.

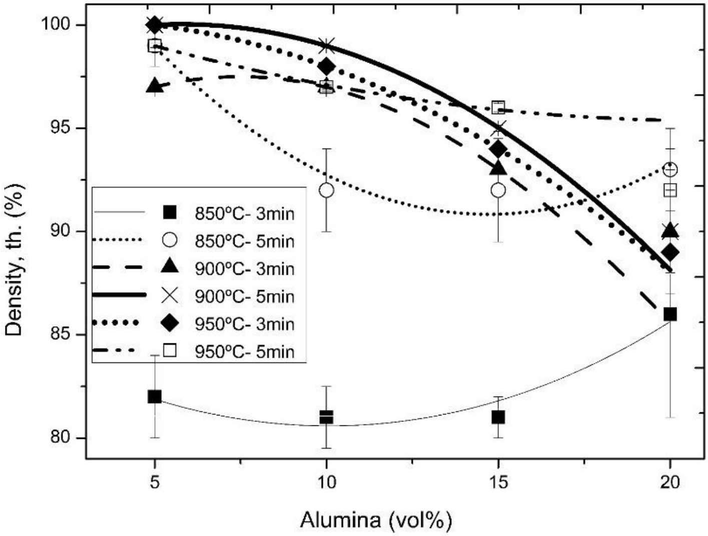

Figure 52. Relative density of alumina-filled borosilicate glass compacts as function of alumina content, fast fired at indicated holding time and temperatures.

The highest relative density was obtained after fast firing borosilicate glass compacts during 5 min at 900°C and for 3 min at 950°C. For alumina-filled borosilicate glass compacts containing 5 vol.% of alumina after fast firing during 5 min at 900°C exhibited de highest density. For alumina content above 5 vol.% densification shows similar behavior observed using conventional sintering and the same origin for this behavior could be addressed.

When compared to conventional sintering (see Fig. 45), a reduction in sinterability of compacts fired at 850 °C can be observed. It is thought, that this temperature is not high enough to create a thermal gradient within the compact to favor mass transport during fast firing up to 7 min.

The microstructure of the samples fast fired at 900 °C for 3 min was analyzed by SEM, and it is shown in Fig. 53.

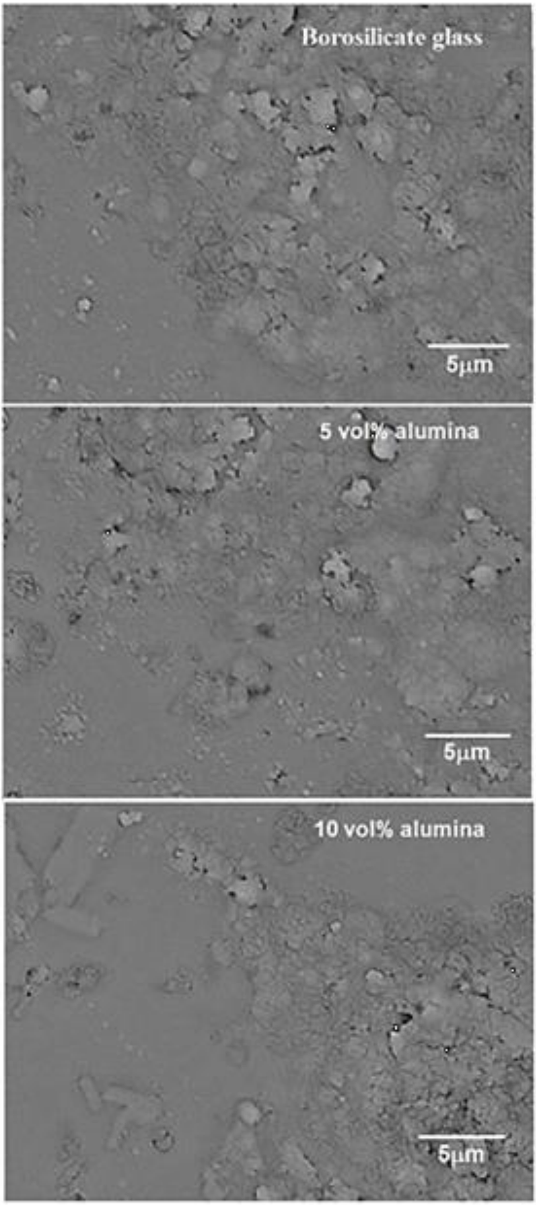

Figure 53. SEM images of borosilicate glass samples fast fired at 900°C for 3 min.

Fig. 53 shows a microstructure with isolated cristobalite agglomerates for both borosilicate glass and composites. Cracks around cristobalite crystals can be observed in a larger amount when compared to conventional sintered samples (see Fig. 49). When compared to conventionally sintered samples, fast fired samples showed the same relative density for composites with 5 vol% considering the error.

5.3 Flexural strength analysis

5.3.1 Conventional sintering

The flexural strength (σ) and Weibull modulus (m) of borosilicate glass and CFG composites containing 5 and 10 vol.% of alumina conventionally sintered during 5 min at 800 °C, heated using heating rate of 15 °C/min, were determined and are shown in Fig. 54.

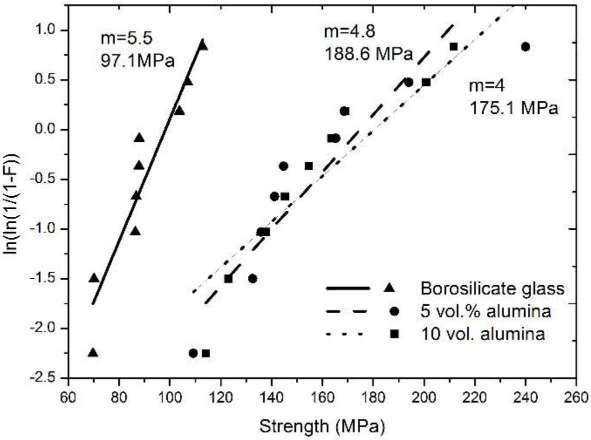

Figure 54. Flexural strength and Weibull distribution of borosilicate glass and CFG composites sintered at 800 ºC, heating rate of 15 ºC/min for 5 min.

Fig. 54 shows an increase of flexural strength of borosilicate glass with alumina addition. The flexural strength of borosilicate glass was 97±15 MPa and for composites containing 5 and 10 vol.% alumina,175 ± 38 MPa and 188 ± 32 MPa, respectively. The Weibull module for borosilicate glass, and composites containing 5 and 10 vol.% alumina were 5.5, 4, and 4.8. The reduction in Weibull module of composites when compared to borosilicate glass samples could be related to alumina agglomeration causing a broad distribution of size defects.

The increase in flexural strength determined in alumina-filled borosilicate composites, could be related to load-transfer due to the presence of high- elastic modulus alumina particles in the glass matrix decreasing the tendency for deformation during loading.[20, 78] Also, the presence of residual compressive internal stresses in the matrix created during cooling due to the thermal expansion mismatch between matrix and inclusions, could have further contributed to the observed increase in strength.[20] Cristobalite formation is lower in composites as shown in Fig. 47, as transformation of β to α cristobalite during cooling creates detrimental stresses, (See section 2.5) the absence of cristobalite could have contributed to the increase in mechanical strength.

5.3.2 Flexural strength analysis of fast fired samples

The flexural strength and Weibull modulus of borosilicate glass and CFG composites containing 5 and 10 vol.% alumina fast fired at 900 ^{o}C for 5 min were determined and are shown in Fig. 55.

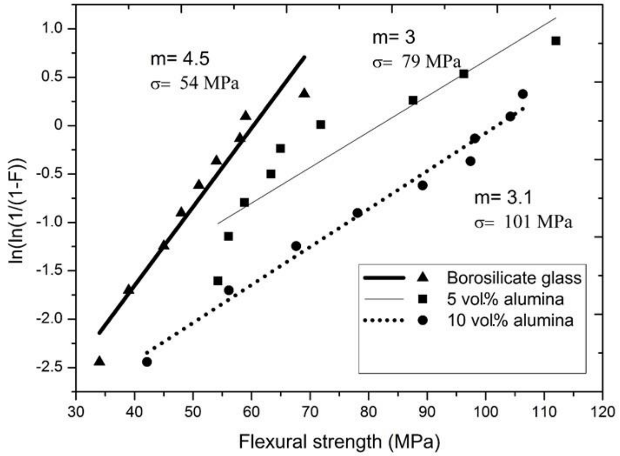

Figure 55. Flexural strength and Weibull distribution of borosilicate glass and CFG composites fast fired at 900^{o}C for 5 min. Composition as indicated.

The flexural strength and Weibull modulus in fast fired samples is lower than those determined for samples fabricated by conventional sintering. The flexural strength of fast fired samples increases with increasing alumina content, but when compared to conventional sintered samples σ was 55% lower (54 ± 10 MPa) for borosilicate glass, and for composites containing 5 and 10 vol.% alumina, 42% (79 ± 16 MPa) and 57% (101 ± 23 MPa) lower, respectively. The Weibull module of the borosilicate glass, and the composites containing 5 and 10 vol.% alumina were 4.5, 3, and 3.1, respectively.

To try to find an explanation for the decrease on mechanical properties of fast fired samples when compared to those obtained by conventional sintering, the formation of cristobalite during fast firing was analyzed by XRD and compared to samples conventionally sintered (see Fig.56).

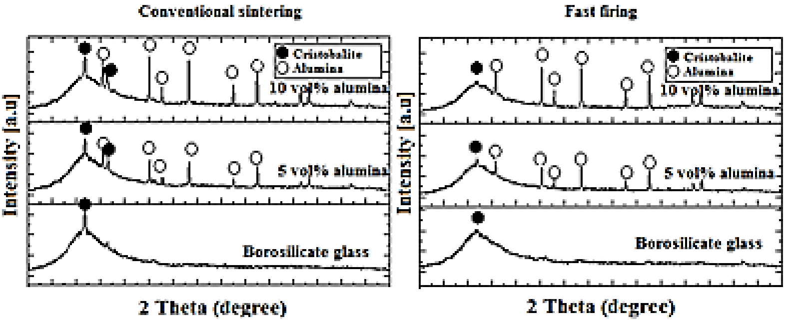

Figure 56. XRD of samples conventional sintered during 5 min at 800°C, heating rate of 15°C/min and fast fired samples at 900°C for 5 min. Composition as indicated.

When compared to fast fired samples, in conventional sintering is observed higher peaks of cristobalite, which can be related to a higher degree in crystallinity.[79] A decrease in cristobalite formation with increasing alumina content can be observed. In fast fired samples, the presence of alumina has not shown any effect on crystallization, probably due to the short time at high temperature used during the entire sintering process. The amount of cristobalite formed during conventional sintering and fast firing seems to be the same and, therefore, the decrease in mechanical properties in fast fired samples cannot be related the amount of cristobalite formed.

Fig. 57 shows SEM images of the microstructure of transversal section of samples conventional sintered (CONV) and fast fired (FF).

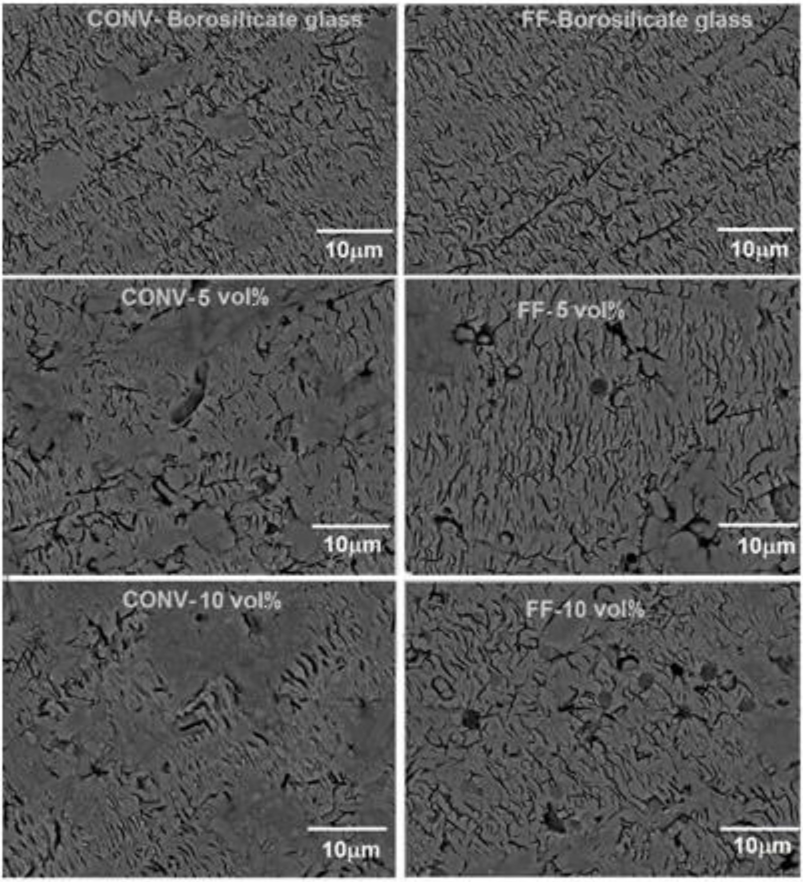

Figure 57. SEM images of samples tested mechanically conventionally sintered during 5 min at 800°C, heating rate of 15°C, and fast fired at 900°C for 5 min.

Fig. 57 shows a surface mostly occupied by cracks related to the stress developed during the test. No difference in the microstructure of samples conventionally sintered and fast fired could be observed.

Although the cause of the difference in mechanical properties between conventional and fast fired samples could not be observed from SEM images and the cause remains elusive, it is thought that it could be related to cristobalite transformation during rapid cooling in fast fired samples. During cooling cristobalite transforms from β to α-cristobalite. The changes in their unit cells, causes a large change in thermal expansion. Inβ-cristobalite, a-axis expands at only 2.1 x 10^{-5} Å $^{o}C^{-l}$; whereas in α-cristobalite the a- and c-axis increase rapidly at rates of 9.3x 10^{-5} and 3.5 x 10^{-5}, Å^{o}C^{-l}, respectively. This behavior translates into very large, spontaneous strains of -1% along a-axis and -2.2% along c-axis during inversion, and could have created microcracks.[6]

The actual transition temperature of cristobalite transformation is dependent upon the degree of crystallinity of the specimen: well-crystallized materials transform at the highest temperatures; and materials which are poorly crystallized have a lower transition temperatures.[80] As shown in Fig. 56, fast fired samples are less crystalline, so the transformation temperature of cristobalite is expected to be lower than in conventional sintered samples. The deformability of borosilicate glass matrix decreases with temperature i.e., is more rigid, and consequently the stress created during the β to α-cristobalite transformation could not be relaxed easily by matrix deformation. Both rapid cooling and the rigidity of the borosilicate glass could have contributed to avoid stress relaxation having as a consequence the formation of microcracks which could have reduced mechanical resistance.

5.4 Fracture toughness analysis

The fracture toughness of borosilicate glass and CFG composites fabricated by conventional sintering was determinate and shown in Table 11.

Table 11. Fracture toughness of borosilicate glass and CFG composites.

Material	K_{Ic} (MPa.m$^{1/2}$)
Borosilicate glass	0.7 ± 0.1
Borosilicate glass + 5 vol.% alumina	1.3 ± 0.1
Borosilicate glass + 10 vol.% alumina	1.9 ± 0.1

Table 11 shows an increase in fracture toughness with alumina content. The crack propagation path in borosilicate glass and composites was analyzed and is shown in Fig. 58.

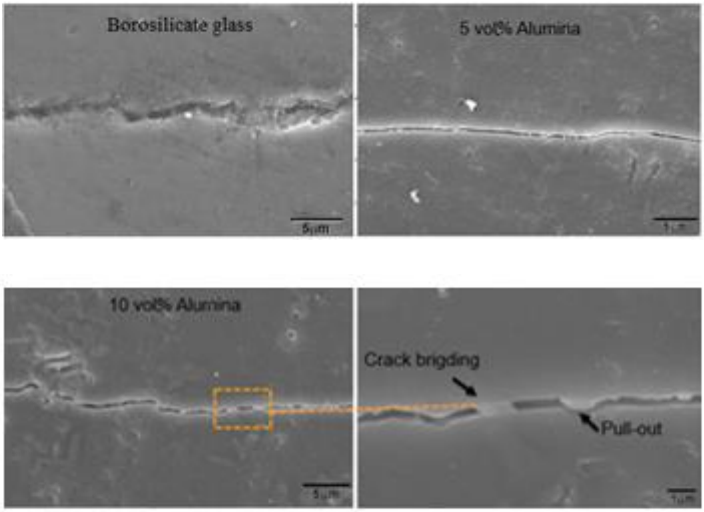

Figure 58. SEM images of crack path in borosilicate glass and CFG composites.

Toughening mechanisms acting upon the crack can be identified by the SEM images. In borosilicate glass the crack propagates practically straight due to the flat surface. In composites, crack deflection, crack bridging and pull-out were observed on the crack propagation path. The observed toughening mechanisms could be related to the thermal expansion coefficient mismatch between alumina (α= $9\times10^{-6}/^{o}$C) and borosilicate glass matrix (α= 3.5×10^{-6} /^{o}C). The development of radial compressive stresses in the matrix around the reinforcement upon cooling is expected and consequently cracks are deflected by alumina particles.

The interface between alumina and borosilicate glass was analyzed by SEM.

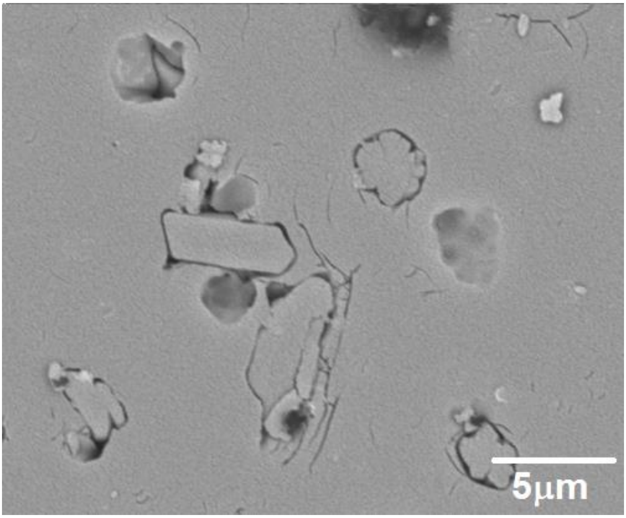

Figure 59.SEM image of conventional sintered alumina-filled borosilicate glass fabricated sintering time 5 min at 800ºC, and heating rate of 15ºC/min.

Fig. 59 shows that alumina and borosilicate glass in CFG-composites form weak interfaces which are probably related to the increase on fracture toughness. Alumina particles are almost detached from the borosilicate glass matrix forming a weak interface. It was not possible to find information in literature about wettability of borosilicate glass on alumina, but the observed small interaction between alumina particle and the glass, could indicate poor wettability. Also, due to the higher CTE of alumina compared to borosilicate glass, the higher retraction of alumina during cooling could have contributed to observed detachment between alumina particles and the glass.

The fracture surface of borosilicate glass and CFG composites was analyzed by SEM and is shown in Fig. 60.

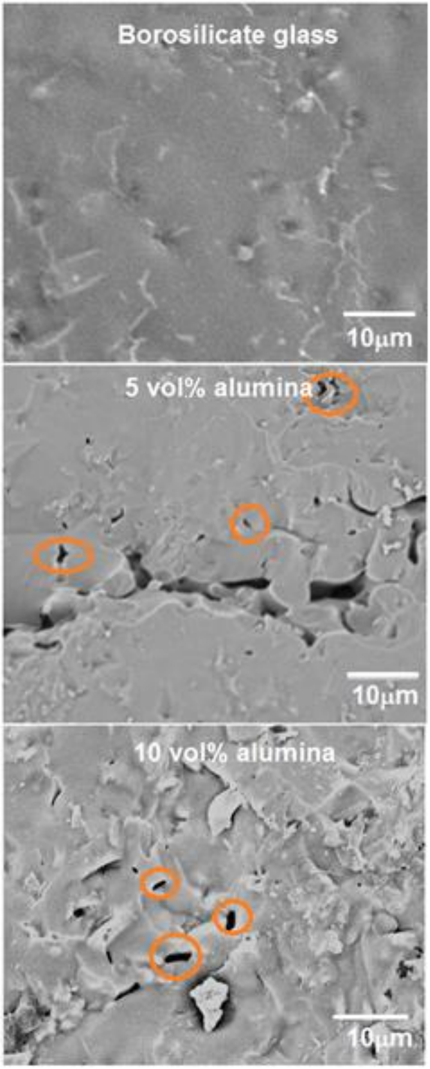

Figure 60. Fracture surface of conventionally sintered borosilicate glass and CFG composites, sintered during 5 min at 800°C, heating rate of 15°C/min. Alumina pull-out indicated by circles.

Examination of SEM images in Fig.60 shows an almost flat borosilicate glass fracture surface indicating that the crack path has not been deflected. An increasing on roughness of the fracture surface for composites containing 5 and 10 vol.% alumina can be observed, indicating that the crack has been deflected. The fracture propagates through the glass matrix around the inclusion. No alumina particles cutting have been observed.

5.5 Vickers hardness analysis

Vickers hardness was determined in fast fired and conventionally sintered samples using Vickers indentation tests at a load of 5N, and the results are shown in Fig. 61.

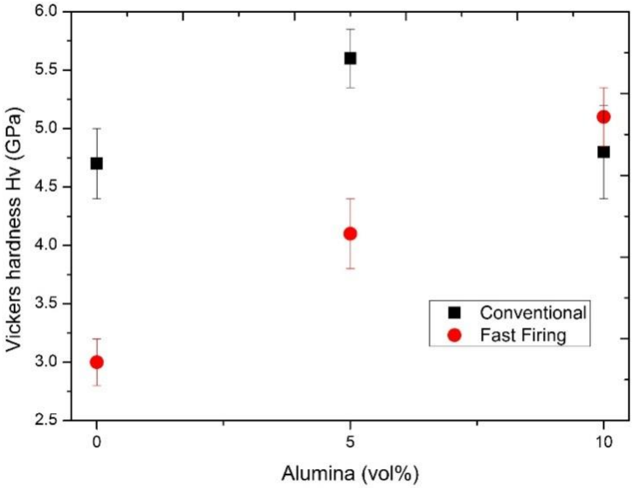

Figure 61. Vickers hardness of samples conventionally sintered during 5 min at 800°C, heating rate of 15°C/min, and fast fired at 900°C for 5 min.

Due to the presence of alumina (Hv = 19 GPa), hardness in composites is higher than borosilicate glass and increases with increasing alumina content. Fast fired samples shown lower hardness when compared to conventionally sintered samples, possibly due to a high amount of microcracks created in fast firing during cooling as explained in section 4.3.2.

5.6 Dielectric constant analysis

Electrical conductivity measurements of borosilicate glass and CFG composite samples were performed and the respective dielectric constant, ε calculated. Results are shown in Table 12.

Table 12. Dielectric constant at 1 MHz.

Material	Dielectric constant(ε) (1 MHz)
Borosilicate glass	5.0 ± 0.5
Borosilicate glass + 5 vol.% alumina	6.5 ± 0.3
Borosilicate glass + 10 vol.% alumina	7.4 ± 0.4

The dielectric constant increases with increasing alumina content. As shown in section 2.11.3, the addition of Al_2O_3 particles leads to changes in glass structure, such as substitution of Si^{4+} by Al^{3+} and glass composition.[5, 23] The difference in the dielectric constant shown in Table 12, from 5 for glass to 7.4 for composites with 10 vol.% is attributed to the presence of Al^{3+} ions in the glass structure acting as modifier. The excess of negative charge originated by the substitution of Si^{4+} by Al^{3+}, is compensated by the Na^+ ions contained in the glass network, maintaining electroneutrality at the local level. As shown in Fig. 62, the ions substitution occurrence causes an increase in the number of dipoles, increasing conductivity. [5, 23]

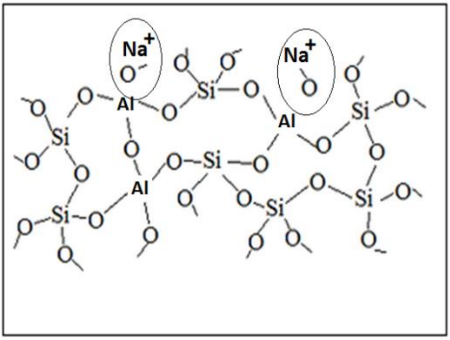

Figure 62. Schematic representation of glass network containing Al^{3+} ions.[23]

5.7 Tape casting of alumina-filled borosilicate mixtures

To study the behavior as tapes of the proposed material containing 5 and 10 vol.% alumina the rheological behavior of the borosilicate glass and mixtures of borosilicate glass and alumina slurries was analyzed. The viscosity was determined for glass and mixtures containing 5 and 10 vol.% alumina, the values were 1098, 1154, 1235 mPa·s, respectively.

The slurries were able to be casted onto the coated carrier, with an easy removal after drying. The tapes presented a smooth and homogeneous surface and good flexibility as shown in Fig. 63. The green relative density of the sheets was approximately 50 th.%, and thickness of 0.9 mm.

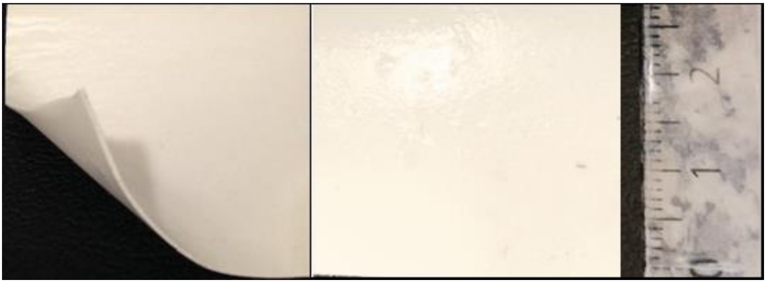

Figure 63. Green tapes of mixtures of borosilicate glass with 5 vol.% alumina content.

Dried tapes were heated up to 500°C in a furnace, with a heating rate of 1°C/min, and debinded for 30 min. Then, using a heating rate of 15°C/min heated up to 800°C and sintered of 5 min. The relative density of the glass and composites containing 5 and 10 vol.% alumina after sintering were 95 ± 5%, 92 ± 6% and 89 ± 5%, respectively, the linear retraction was 17 ± 0.5% for composites containing 5 vol.% alumina, and 16.0 ± 0.7% for composites containing 10 vol.% alumina. Fig. 64 shows the tape with 5 and 10 vol.% alumina after sintering. Thickness of the sintered tapes was ~0.75 mm.

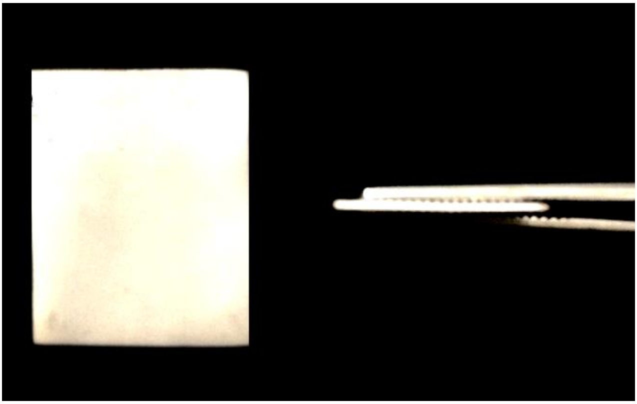

Figure 64. Alumina-filled borosilicate glass tape containing 5 vol.% alumina, after sintered at 800°C for 5 min.

6. CONCLUSIONS

- Uniaxial pressed compacts and tapes of borosilicate glass and alumina-filled borosilicate glass composites were fabricated by conventional sintering and uniaxial pressed compacts by fast firing and the relation between processing parameters and final density were studied.
- The optimized processing parameters for conventional sintering which achieved the highest relative density with the mechanical properties suitable to use as substrate for microelectronic packaging were a heating rate of 15ºC/min, holding time of 5min, sintering temperature of 800ºC, glass particle size of $D_{50} = 20\mu m$ and alumina particle size of $D_{50} = 3\mu m$.
- Increasing the heating rate, increases densification and inhibit cristobalite formation in conventionally sintered borosilicate glass.
- Alumina hinders cristobalite formation in borosilicate glass during conventional sintering.
- Alumina addition increases flexural strength and fracture toughness of conventionally sintered borosilicate glass.
- Alumina addition increases fracture toughness of borosilicate glass by crack deflection, crack bridging and pull-out.
- Alumina addition increases hardness, dielectric constant and coefficient of thermal expansion of conventionally sintered borosilicate glass.
- Alumina addition has no effect on cristobalite formation during fast firing.
- Flexural strength of fast fired borosilicate glass and alumina-filled borosilicate glass composites decreased when compared to conventionally sintered samples due to, possibly, the presence of microcracks originated during rapid cooling by $\beta \rightarrow \alpha$ cristobalite transformation.

- Hardness of fast fired samples decreased when compared to conventionally sintered, probably due to microcracks formation.

7. Appendix 1

7.1 Nucleation rate

For nucleation in condensed phases, close to the equilibrium melting temperature, T_m, the free-energy change per unit volume on transforming phases, ΔG_v, is approximately proportional to the difference between the melting and crystallization temperature, ΔT, i. e., the degree of undercooling.[2] The free-energy change per unit volume can be calculated using equation 23:

$$\Delta G_v \approx \frac{\Delta H_v \Delta T}{T_m} \tag{23}$$

where ΔH_v is the heat of transformation per unit volume. The overall change in free energy, $\Delta G_{(v)}$, for phase transformation is the sum of energy required to the formation of the interface and the change in volume free energy related to the phase transformation $\alpha \rightarrow \beta$. Considering a spherical nucleus with radius r, the free energy change is

$$\Delta G_{(r)} = 4\pi r^2 \gamma_{SL} + \frac{4}{3}\pi r^3 \Delta G_v \tag{24}$$

where γ_{SL} is the interface energy.

The critical size of the embryo that has the maximum free energy, ΔG^* and which leads to a continuous growing in size and decrease in free energy (see Fig. 4) is given by[2]

$$r^* = -\frac{2\gamma_{SL}}{\Delta G_v} \quad (25)$$

7.2 Homogeneous nucleation rate

The nucleation of most phase transformation takes place heterogeneously on substrates which reduce the thermodynamic barrier to nucleation. Substituting r^* into equation 24, the energy barrier associated to homogeneous nucleation, ΔG^* can be calculated by[2]

$$\Delta G^* = \frac{16\pi\gamma_{SL}^3}{3\Delta G_v^2} = \frac{16\pi\gamma_{SL}^3 T_m^2}{\Delta H_v^2 \Delta T^2} \quad (26)$$

The steady-state nucleation rate per unit volume is defined as

$$I = \varphi n^* \quad (27)$$

where n^* is the steady-state population of critical nuclei per unit volume (m^{-3}), and φ is the frequency factor or rate at which atoms join critical nuclei (s^{-1}).

$$n^* = n_0 exp(-\Delta G^*/kT) \quad (28)$$

n^* depends on both the absolute temperature, T and the undercooling, ΔT.

$$\phi = \omega \; exp(-\Delta G_m/kT) \quad (29)$$

where n_0 is the single molecules per unit volume, k the Boltzmann constant, ω the atomic vibrational frequency and ΔG_v, is the activation energy for atomic migration.[2]φ can be written by an alternative form considering the melt viscosityη.

$$\varphi = \frac{kT}{3\pi a_0 \eta} \tag{30}$$

Substituting ΔG^* in Eq.24 for ΔG^* in equation 29, the homogeneous nucleation rate I, can be calculated using equation 31:

$$I = n_0 \omega exp \frac{-16\pi\gamma^3 T_m^2}{3kT\Delta H_v^2 (T_m - T)^2} exp\left(-\frac{\Delta G_m}{kT}\right) \tag{31}$$

7.3 Heterogeneous nucleation rate

For the steady-state heterogeneous nucleation, the free energy for forming a critical-size embryo having the shape of a spherical cap on a substrate is given by

$$\Delta G_{het}^* = \Delta G^* f(\theta) \tag{32}$$

where ΔG_{het}^* is the free energy barrier to heterogenous nucleation, ΔG^* the energy barrier to form an embryo of a critical size.

$$f(\theta) = \frac{(2+\cos\theta)+(1-\cos\theta)^2}{4} \tag{33}$$

where θ is the contact angle between substrate and nucleus. The thermodynamic barrier for nucleation on a substrate decreases with θ. The steady-state heterogeneous nucleation rate per unit *area* of substrate, I_s, in condensed phases is

$$I_s = K_s exp\left(\frac{-\Delta G_{het}^*}{kT}\right) \tag{34}$$

where

$$K_s \approx n_s^0 \omega exp\left(\frac{-\Delta G_{het}^*}{kT}\right) \tag{35}$$

The expression is similar to homogenous nucleation rate, however the number of molecules is per unit $area,n_s^0$, due to the contact with substrate, instead of molecules per unit volume for homogeneous nucleation.

7.4 Crystal growth

After a stable nucleus has been formed, the rate of growth is determined by the rate at which material reaches the nucleus-melt interface that depends on the temperature and the degree of supersaturation of the melt.[81]

The growth rate per unit area of the nucleus-melt interface, u, can be calculated by equation 36

$$u = \varphi a_0 \left[1 - exp\left(-\frac{\Delta G}{kT}\right)\right] \tag{36}$$

where a_0 is the thickness of the layer on the interface and is the molecular diameter of the constituted nucleus composition.

8. REFERENCES

1. PASCUAL, M.J.; PASCUAL, L.; DURÁN A. **Modelling of sintering process in borosilicate glasses with rigid inclusions**. European Society of Glass Science and Technology, 2002.

2. KINGERY, W. D.; BOWEN, H. K.; UHLMANN D. R. **Introduction to ceramics**. 2nd ed. New York: John Wiley & Sons, 1976.

3. EWSUK, K.G.; HARRINSON, L.W.; WALCZAK, F.J. **Sintering glass-filled ceramic composites;effects of glass properties**. Ceram. Transactions**,** v. 1, p. 969-977, 1988.

4. RAJ, R.; BORDIA, K. **Sintering behavior of bi-modal powder compacts**. Acta Metall.**,** v. 32, p. 1003-1019, 1984.

5. JEAN, J. H.; KUAN, T. H. **Crystallization inhibitors during sintering of Pyrex borosilicate glass**. J. Mater. Sci. Lett.**,** v. 14, p. 1068-1070, 1995.

6. HOLAND, W.; BEALL, G. **Glass-ceramics technology**. 1st ed. Westerville: The American Ceramic Society, 2002.

7. E. BERNARDO, G. SCARINCI **Sintering behaviour and mechanical properties of Al_2O_3 platelet-reinforced glass matrix composites obtained by powder technology**. Ceramics International**,** v. 30, p. 785-791, 2004.

8. PARK, S. J.; LEE, S. J. **Mechanism of preventing crystallization in low-firing glass/ceramic composite substrates**. J. Am. Ceramic. Soc.**,** v. 78, n. 4, p. 1128-1130, 1995.

9. EL-KHESHEN, A. A. **Effect of alumina addition on properties of glass/ceramic composite**. Brit. Ceram. Trans.**,** v. 102, n. 5, p. 205-209, 2003.

10. L.W. HARRISON, K.G. EWSUK **Processes for manufacturing tailored property ceramic composites, in design for manufacturability and manufacture of ceramic components**. The American Ceramic Society, Westerville, OH, Ceram. Trans.**,** v. 49, p. 197-219, 1995.

11. EWSUK, K.G.; HARRINSON, L.W. **Densification of glass-filled alumina.** . Sintering of advanced ceramics in Advances in Ceramics v. 7, p. 438-451, 1990.

12. KAGAWA, Y.; KOGO, Y.; HATTA H. **Thermal expansion behavior of the Si,N,-whisker-reinforced soda-borosilicate glass matrix composite**. J. Am. Ceram. Soc.**,** v. 72, n. 6, p. 1092-1094, 1989.

13. BOCCACCINI, A.R.; JANCZAK-RUSCH, J.; PEARCE, D.H.; KERN H. **Assessment of damage induced by thermal shock in SiC-fiber-reinforced borosilicate glass composites**. Composites science and technology**,** v. 59, p. 105-112, 1999.

14. KLUG, T.; BRUCKNER, R **Preparation of C-fibre borosilicate glass composites: Influence of the fibre type on mechanical properties**. J. Mat Sci.**,** v. 29, p. 4013-4021, 1994.

15. DURAN, A.; PASCUAL, M. J.; PASCUAL, L. **Sintering behaviour of composite materials borosilicate glass-ZrO2 fibre composite materials**. J. eur. Ceram. Soc.**,** v. 22, p. 1513-1524, 2001.

16. JEAN, J. H.; LIN, S. **Effects of borosilicate glass on densification and properties of borosilicate glass + TiO2 ceramics**. J. Mater. Res.**,** v. 14, n. 4, p. 1359-1363, 1999.

17. RAY, A.; TIWARI, A.N. **Compaction and sintering behaviour of glass–alumina composites**. Materials Chemistry and Physics**,** v. 67, p. 220-225, 2001.

18. LIU, M.; HONGQING, Z.; HAIKUI, Z.; ZHENXING, Y. JIANXIN, Z. **Microstructure and dielectric properties of glass/Al2O3 composites with various low softening point borosilicate glasses**. J. Mater. Sci.: Mater. Electron.**,** v. 23, p. 2130-2139, 2012.

19. JEAN, J.; GUPTA, T. K. **Effect of alumina on densification of binary borosilicate glass composite**. J. Mater. Res.**,** v. 9, n. 8, p. 1990-1996, 1994.

20. BOCCACCINI, A. R.; TRUSTY, P. A. **Toughening and strengthening of glass by Al203 platelets**. , J. Mater. Sci. Lett**,** v. 15, p. 60-63, 1996.

21. ZAWRAH, M. F.; HAMZAWY, E. M. A. **Effect of cristobalite formation on sinterability, microstructure and properties of glass/ceramic composites**. Ceram. Int.**,** v. 28, p. 123-130, 2002.

22. MONTEIRO, R.C.C.; LIMA, M.M.R.A. **Effect of compaction on the sintering of borosilicate glass/alumina composites**. j. eur. Ceram. Soc.**,** v. 23, p. 1813-1818, 2003.

23. LIMA, M.M.R.A.; MONTEIRO, R.C.C.; GRAÇA, M.P.F.; FERREIRA DA SILVA, M.G. **Structural, electrical and thermal properties of borosilicate glass–alumina composites**. J. of Alloys and Compounds**,** v. 538, p. 66-72, 2012.

24. YET-MING CHIANG, DUNBAR BIRNIE III AND W. DAVID KINGERY **Physical Ceramics: Principles for Ceramic Science and Engineering**.ed. New York: J. Willey, 1997.

25. REED, J.S. **Principles of ceramic processing**. 2nd ed. New York: Willey, 1995.

26. F. VARNIK, A. RIOS, M. GROSS AND I. STEINBACH **Simulation of viscous sintering using the lattice Boltzmann method**. Modelling Simul. Mater. Sci. Eng. United Kingdom. 21 2013.

27. RAHMAN, LUTGARD C. DE JONGHE AND MOHAMED N. **Sintering of Ceramics**. In: AL., S. SOMIYA ET (Ed.). **Handbook of Advanced Ceramics**: Elsevier Inc., 2003. cap. 4,

28. DE JONGHE, L. C.; RAHAMAN, M.N. **Sintering of Ceramics**.ed. Elsevier Inc., 2003.

29. KANG, S. L. **Sintering, densification, grain growth and microstructure**. 1st ed. Oxford: Elsevier Butterwortj-Heinemann, 2004.

30. RAHAMAN, M. N. **Ceramic processing and sintering**. Second ed. New York: Marcel Dekker, 2003.

31. ZANOTTO, M. O. PRADO AND E. D. **Glass sintering with concurrent crystallization**. C. R. Chimie, 2002.

32. M. O. PRADO, E. B. FERREIRA AND E. D. ZANOTTO **Sintering kinetics of crystallizing glass particles. A review**.

33. BORDIA, R. K.; CAMACHO-MONTES, H. **Sintering: Fundamentals and Practice**.ed. New York: John Wiley & Sons, Inc., 2012.

34. REIS, RAPHAEL MIDEA CUCCOVIA VASCONCELOS. **Avaliação de modelos de sinterização por fluxo viscoso e determinação da taxa de crescimento de cristais e fração cristalizada em vidros**. 2012. 134 Science and Engineering of Materials, Universidade Federal de São Carlos, São Carlos.

35. M. J. PASCUAL, A. DURÁN, L. PASCUAL **Sintering behaviour of composite materials borosilicate glass-ZrO2 fibre composite materials**. Journal of the European Ceramic Society**,** v. 22, p. 11, 2001.

36. M. D. SACKS, R. RAUGHUNATHAN, I. Y. PARK AND G. W. SCHEIFFELE **Processing and Properties of Glass/Ceramic Composites with Low Dieletric Constant Prepared from Mircrocomposite Particles**. In: (Ed.). **Materials in Microelectronic and Optoelectronic Packaging (Ceramic Transactions)**. Westerville: Aerican Ceramic Societty, v.33, 1993.

37. EWSUK, K. G. **Sintering maps for ceramic-filled-glass composites**.

38. WANG, D. N. K. **Sintering of Al2O3 Power Compact by Hot Stage-Scanning ElectronMicroscopy**. 1976. University of California, Berkeley.

39. CHU, M. Y.; RAHAMAN, M. N.; DE JONGHE, L. C.; BROOK, R. J. **Effect of Heating Rate on Sintering and Coarsening**. J. Am. Ceram. Soc, v. 74, p. 1217-1225, 1991.

40. LANGE, F. F. **Approach to Reliable Powder Processing**. Ceramic Transactions, American Ceramic Society, v. 1, p. 1069-1083, 1989.

41. GARCÍA, D. E.; KLEIN, A. N.; HOTZA, D. **Advanced Ceramics with dense and fine-grained microstructures through fast firing**. Rev. Adv. Mater. Sci., v. 30, p. 273-281, 2012.

42. D.E. GARCIA, D. HOTZA, R. JANSSEN **Building a sintering front through fast firing**. International Journal of Applied Ceramic Technology, v. 8, p. 1486-1493, 2011.

43. MOSTAGHACI, H.; BROOK R.J. **Production of dense and fine grain size BaTiO3 by fast firing**. Trans. J. Br. Ceram. Soc., v. 82, n. 5, p. 167-170, 1983.

44. MOSTAGHACI, H.; BROOK, R. J. **Fast Firing of Non-Stoichiometric BaTiO3**. Trans. Br. Ceram. Soc., v. 80, n. 5, p. 148-149, 1981.

45. RAHAMAN, M. N. **Ceramic processing and sintering**. 2nd ed. New York: Marcel Dekker, 2003.

46. GRESKOVICH, C.; LAY, K.W. **Grain Growth in Very Porous Al2O3 Compacts**. J. Am. Ceram. Soc.**,** v. 55, n. 3, p. 142-146, 1972.

47. KIM, D. H.; KIM, C. H. **Effect of Heating Rate on Pore Shrinkage in Yttria-Doped Zirconia**. J. Am. Ceram. Soc.**,** v. 76, n. 7, p. 1877-1888, 1995.

48. POSSAMAI, T.S.; OBA, R.; NICOLAU, V.P.; HOTZA, D.; GARCIA, D.E.; HALLORAN, J. **Numerical Simulation of the Fast Firing of Alumina in a Box Furnace**. J. Am. Ceram. Soc., p. 1-8, 2012.

49. CALLISTER, W. D. **Materials science and engineering an introduction**. 8th ed. New York: John Wiley & Sons, 2009.

50. SHARTIS, C. L. **Density, expansivity and viscosity of molten alkali silicate**. National Bureau of standards, p. 155-160, 1952.

51. MARINO, L. F. B **A expansao térmica de materiais cerâmicos-Parte II: Efeito das condições de fabricação**. Cerâmica Industrial**,** v. 3, n. 3, p. 23-33, 1998.

52. UHLMANN, D. R. **The thermal expansion of alkali borate glasses**. J. Now-Crystal. Solids**,** v. 1, p. 347-359, 1969.

53. KASTELEYN, P. W.; FORTUIN, C. M. **Phase transition in lattice systems with random local properties**. J. Phys. Soc. Japan**,** v. 26, p. 11-14, 1969.

54. DIETRICH S. , AMNON A. **Introduction to percolation theory**. 2nd ed. New York: Taylor and Francis, 1992.

55. CHENG-HUA, K.; GUPTA, P.K. **Rigidity and conductivity percolation threshold in particulate composites**. Acta Metall. Mater.**,** v. 43, p. 397-403, 1995.

56. BASU, B.; VLEUGELS, J.; DER BIEST, O.V. **Development of ZrO2–TiB2 composites: role of residual stress and starting powders**. J. Alloy. Compd.**,** v. 365, p. 266-270, 2004.

57. XU, C. **Effects of particle size and matriz grain size and volume fraction of particles on the toughening of ceramic composite by thermal residual stress**. Ceram. Int., p. 537-542, 2005.

58. YAN, Z.; MARTIN, C.L.; GUILLON, O.; BOUVARD D. **Effect of size and homogeneity of rigid inclusions on the sintering of composites**. Scripta Materialia**,** v. 69, p. 327-330, 2013.

59. LANGDON, L.G.; XIA K. **The toughening and strengthening of ceramic materials through discontinuous reinforcement**. J. Mater. Sci.**,** v. 29, p. 5219-5231, 1994.

60. . LTD., PLEXTEK RF INTEGRATION PLEXTEK. London Road, Great Chesterfod, Essex.

61. IMANAKA, I. **Multilayered low temperature cofired ceramics (LTCC) technology**.ed. Boston: Springer, 2005.

62. SURENDRAN, R. ET AL. **Low Temperature Sintering and Dielectric Properties of Alumina-Filled Glass Composites for LTCC Applications**. Int. J. Appl. Ceram. Technol.**,** v. 9, n. 1, p. 52-59, 2012.

63. THICK-FILM SENSORS, EDITED BY M. PRUDENZIATI, ELSEVIER, 1994, 59-71.,

64. BIROL, H. **Fabrication of low temperature co-fired ceramic (ltcc)-based sensor and micro-fluidic structures**. 2007. (PhD). École Polytechnique Fédérale de Lausanne, Faculté des Science et Techniques de L'Ingenieur, Lausanne.

65. CYNTHIA, G. ET AL. **Laminated object manufacturing of LZSA glass-ceramics**. Rapid Prototyping J.**,** v. 17, n. 6, p. 424-428, 2011.

66. BANNISTER, M. **Science and technology of zirconia** 1st ed. Pensilvania: Technomic, 1993.

67. RICHERSON, D. W. **Modern ceramic engineering, properties, processing and use in design**. 2nd ed. New York: John Wiley & Sons, 1992.

68. WEIBULL, W. **A statistical distribuition function of wide applicability**. J. Appl. Mech.**,** v. 18, p. 293-297, 1951.

69. HERTZBERG, R. W. **Deformation and fracture mechanics of engineering materials**. 4th ed. New York: John Wiley & Sons, 1995.

70. BARSOUM, M.W. **Fundamentals of ceramics**. 1st ed. Bristol: IOP Publishing Ltd., 2003.

71. LAWN, B.R.; E. R. FULLER, E.R.; WIEDERHORN S.M. **Strength degradation of brittle surfaces: sharp indenters**. J. Am. Ceram. Soc.**,** v. 59, n. 5-6, p. 193-197, 1976.

72. AGILENT TECHNOLOGIES, INC. 2013 – 2014, PUBLISHED IN USA, MAY 16, 2014 5989-2589EN

73. **Composition of pyrex glass, National Institute of Standarts and Technology,2000.** .

74. RACHADEL, P. L.; BIROL, H.; OLIVEIRA, A.P.N.; HOTZA, D. **Development of Alternative Glass Ceramic Seal for a Planar Solid Oxide Fuel Cell**. Advances in Materials Science Engineering**,** v. 2012, p. 1-6, 2012.

75. LIMA, M.M.; MONTEIRO, R. **Characterization and thermal behaviour of a borosilicate glass**. Thermochimica Acta**,** v. 373, p. 69-74, 2001.

76. A. R. BOCCACCINI, E. A. OLEVSKY **Processing of platelet-reinforced glass matrix composites: effect of inclusions on sintering anisotropy**. J. Mater. Process. Tech**,** v. 96, p. 92-101, 1999.

77. PRUYN, T. L.; GERHARDT, R. A. **Percolation in Borosilicate Glass Matrix Composites Containing Antimony-Doped Tin Oxide Segregated Networks. Part II: Examination of Electrical Behavior Using Impedance Spectroscopy**. J. Am. Ceram. Soc**,** v. 97, n. 7, p. 2082-2090, 2014.

78. ZAWRAH, M. F. M.; EL-KHESHEN, A. A **Characterisation of borosilicate glass matrix composites reinforced with SiC or ZrO2**. Brit. Ceram. Trans.**,** v. 103, n. 4, p. 165-170, 2004.

79. WOLFENDEN, A.; THOMAS, H.M.; THOMAS, V.; CHAWLA, K.K. **Measurement of young's modulus and damping as a function of temperature in a borosilicate glass-matrix composite with continuous ceramic fibres**. J. Mater. Sci. Lett.**,** v. 14, n. 22, p. 1555-1557, 1995.

80. CHANG-JUN, B. **Integrally cored ceramic investiment casting mold fabricated by ceramic**. 2008. Materials science and engineering, Michigan

81. MERSMANN, A. **Crystallization Technology Handbook**. 2nd ed. New york: 2001.